IEEE Access
Multidisciplinary | Rapid Review | Open Access Journal

Received 12 December 2022, accepted 24 January 2023, date of publication 30 January 2023, date of current version 2 February 2023.

Digital Object Identifier 10.1109/ACCESS.2023.3240516

RESEARCH ARTICLE

Grid-Forming Control of Voltage Source Converters Based on the Virtual-Flux Orientation

JOSÉ LUIS RODRÍGUEZ-AMENEDO[1], (Senior Member, IEEE), SANTIAGO ARNALTES GÓMEZ[1], MARKEL ZUBIAGA[2], PEDRO IZURZA-MORENO[2], JOSEBA ARZA[2], AND JUAN DOLADO FERNÁNDEZ[1]

[1]Electrical Engineering Department, University CARLOS III of Madrid, Leganés, 28911 Madrid, Spain
[2]Ingeteam Research and Development Europe S. L., 48170 Zamudio, Spain

Corresponding author: José Luis Rodríguez-Amenedo (amenedo@ing.uc3m.es)

ABSTRACT The increasing penetration of renewable generation in power systems is causing growing concern about system stability. Grid-forming (GFM) control has been appointed as the technology required for achieving a high penetration of renewables in the grid, as it successfully contributes to the power system stability. This paper proposes a novel grid-forming control scheme for voltage source converters (VSC) achieving the operational characteristics of a virtual synchronous machine (VSM). The proposed scheme is based on the orientation of a defined virtual flux to a reference axis obtained from the emulation of the synchronous generator swing equation. The virtual flux is obtained by the integration of the VSC internal voltage and it is oriented to the reference axis by means of a flux controller that also controls the flux magnitude. In this way, the VSC synchronism is maintained, operating as a voltage source connected to the grid. Moreover, the flux orientation in turn allows to control the VSC active power, while the flux magnitude control allows to regulate the VSC reactive power or terminal voltage in isolated mode. The paper also demonstrates that the stability of GFM converters is negatively affected when emulating high inertia values. So, a stabilizer is also proposed for damping these modes. Finally, due to fact that GFM converters behave as voltage sources, their low voltage ride through capability becomes an issue, because they naturally respond to faults with high short-circuit currents, that cannot be withstand by power electronics converters. Therefore, a method for limiting fault currents is proposed as well in the paper. The proposed grid-forming control scheme has been implemented in a real-time control platform and validated using comprehensive simulation models in a real-time simulator for assessing its grid-forming capability.

INDEX TERMS Grid-forming power converter, virtual-flux orientation, virtual synchronous machines.

I. INTRODUCTION

It is a well-known fact that power generation has changed significantly due to the massive integration of renewable energy sources (RES) in power systems worldwide. Renewable power plants are mainly based on inverter-based resources (IBR) for their grid connection, unlike conventional synchronous generators (SG) that use an electromechanical device for such a purpose.

According to the International Renewable Energy Agency (IRENA) [1] more renewable power capacity was added to the grid annually than all fossil fuels and nuclear combined between 2013 a 2020. Renewable power technologies now dominate the global market for new electricity generation capacity. So, it can be concluded that electricity generation growth based on RES in detrimental of non-renewables power plants is a fact nowadays. It seems clear that electrical systems are moving from classical centralized power system where large synchronous generators (SG) units ensure power stability and robustness, towards a decentralized power system where the generation shifts into the distribution level. This type of generation is based on IBR that can be grouped into two categories: a) grid-following converters (GFLs) and b) grid-forming converters (GFCs).

GFL inverter controls are used in most grid-connected IBRs today. These converters typically use a phase-locked

The associate editor coordinating the review of this manuscript and approving it for publication was Md. Rabiul Islam.

loop (PLL) and a fast-current controller. A PLL is used to synchronize the IBR ''following'' the grid voltage by extracting its phase information. This angular position of the grid voltage vector is needed for the internal current control loops. For that reason, GFL-VSC converters are considered as controlled current sources. Due to its control structure, GFL control cannot instantaneously respond to load changes on the grid as it is the case of SGs. There is always an inherent delay in the GFL-VSC response caused by the PLL, so that IBR's active and reactive currents are injected when the disturbance has passed. In addition, it has been shown that GFLs can become unstable under certain low-strength systems [2], [3]. As a consequence of SG declining due to the high penetration of GFL converters in power systems, GFM converters arise as a promising alternative to solve the shortcomings of GFL converters.

GFM controls have the main purpose of maintaining internal voltage phasor in the sub-transient and transient time frame [4]. This allows the IBR to immediately respond to changes in the external network maintaining stability during severe disturbances. Besides, the internal voltage vector must be controlled to maintain synchronism with other generators by regulating active and reactive power appropriately to support the grid. GFM-VSC are recommended to provide some services such as, operation in low system-strength conditions, grid frequency and voltage stabilization, power oscillations damping, re-synchronization capability, system restoration and black-start [5].

Different GFM-VSC controllers can be found in the literature. According to its principle of operation, they can be classified into three categories [6]. The first category includes droop controls, which allow parallel operation of multiple converters emulating the governor action of SGs. This category, in turn, can be subdivided into frequency-based droop [7], [8], [9], [10], [11], [12], angle-based droop [13], [14], [15] and power synchronization control (PSC) [16], [17]. One of the most important drawbacks of droop controls is their lack of inertial response. Recently, a new GFM-VSC controllers' category, named as synchronous-machine-based, has been proposed, whose control provide inertial response and damping. The first attempt of emulating the behavior of a SG was introduced as a concept known as virtual synchronous machine (VISMA) [18], [19]. VISMA systems aim to emulate by control the dynamic equations of a SG. In this category some controllers try to emulate only the SG's swing equation [20], [21], [22], [23], [24], [25], [26], [27], [28], [29], [30], while others operate as virtual synchronous generators (VSG) with augmented capabilities [31], [32], [33], [34], [35], [36], [37], [38] in order to achieve better damping and improved transient stability. Another variant is the so-called Synchronverter which consists of fully reproducing the dynamic equations of the SG including the electrical equations, speed governor and voltage regulator [39], [40], [41], [42], [43], [44]. Lastly, a novel controller is used in [45], [46], and [47] to match the electromechanical energy transfer of SGs by using the DC-link dynamics of the converter. The third category includes some non-linear synchronization methods such as the virtual oscillation-based method [48], [49], [50], [51], [52], [53], [54], [55], [56], [57]. The Virtual Oscillator Controller (VOC) is a non-linear controller that makes the GFM-VSC reproduce the dynamics of a weakly non-linear limit-cycle oscillator allowing the synchronization of several converters running in parallel regardless of their initial operating state. In addition, VOC performs synchronization in a stationary reference frame without the need to determine any control angle by means of a synchronization loop.

On the other hand, as indicated in the literature, [58], [59] there are basically two methods of limiting the current in a GFM-VSC during a voltage dip or severe disturbances in the grid: switching the control mode to a GFL mode during the fault, or limiting the current by using virtual impedances. In the first case, IBR loses all functionalities of the grid-forming control during the fault periods and uses a back-up PLL for the synchronization [60], [61], [62], which has its own stability issues in weak-grids. Current limiting can be achieved directly by saturating the regulators of the inner current loops (if GFM-VSC uses a current regulator), however this causes a reduction of the synchronous stability margin [63] and a wind-up effect in the outer power loop which can lead to instability [64]. To avoid this, some researchers propose the use of virtual resistors, either linear [65] or nonlinear [66]. Also, the influence of the virtual impedance on the grid-forming control for current limitation is analyzed in [67], where it is shown that the current limitation is largely depending on the fault location and the selected virtual impedance. It has also been shown that the use of virtual impedances can lead to stability problems in parallel operation [66]. However, improved virtual impedance methods have been proposed, such as the one reported in [67], which uses a new current limiting method based on the threshold virtual impedance (TVI) during balanced and unbalanced faults.

Therefore, GFM-VSC act as real voltage sources where the internal voltage is kept under control. The module of this internal voltage is determined by an external reactive power control loop, or a voltage regulator, and the voltage angle is controlled by a synchronization loop using the active power. On the one hand, this mode of operation is similar to that of a SG, and has certain advantages such as simplicity. However, it has some disadvantages in regards to its dynamics. In this configuration, no system state variable is directly controlled, which means a lack of robustness. In order to solve this problem, a scheme of several cascaded controllers has been proposed, with a current inner loop and a voltage outer loop [28]. Although it improves the dynamic robustness, the setting of several cascaded controllers has the drawback of slowing down the dynamic response of the system [68].

This paper presents a novel solution using a scheme without any internal current control loops and regulating a

state variable, called virtual-flux, that is obtained as a function of the output current and the integral of the voltage measured at converter's terminals. This virtual-flux is proportional to the internal voltage, so that the control of the converter is achieved in a simple and robust way. In the past, virtual-flux was proposed for inverter droop control in microgrids [69], also using direct control in three-phase rectifiers [70], and applying predictive control [71]. Unlike these proposals, the present virtual-flux control is used to perform a GFM control. In addition, in this work a novel active and reactive current limitations are proposed, as well as a power stabilizer in order to avoid power oscillations produced when designing the GFM-VSC with a high inertia constant and a low damping factor.

This paper is organized as follows. The VSC system description is presented in Section II. The dynamic electric equations of the power converter are also presented by using virtual-fluxes as state-variables. Section III is aimed to the GFM-VSC control by orientation of the virtual-flux vector to a rotating reference frame. This section also includes the small-signal stability analysis and the flux regulators tuning. Section IV shows a method for obtaining the system control angle using an active power synchronization loop including a power stabilizer (PSS) and an active current limiter. Likewise, in Section V a reactive-power/voltage controller with a reactive current limiter are presented. In Section VI the synchronization process is addressed. Subsequently, in Section VII results of a comprehensive real-time simulation are shown and discussed. The complete GFM-VSC control is executed using a hardware-in-the-loop (HiL) experimental set-up connected to a real-time digital simulator (RTDS) where the response of the VSC is analyzed under different grid disturbances. Finally, in Section VIII the final conclusions of this work are presented.

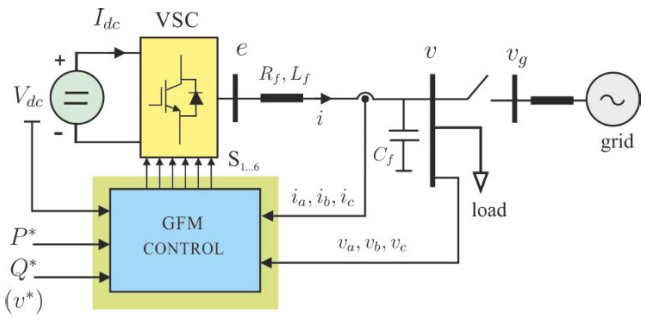

FIGURE 1. System description of a GFM-controlled VSC.

II. SYSTEM DESCRIPTION

Fig. 1 shows the schematic of a three-phase VSC connected to a grid using an LC filter, with parameters R_f, L_f and C_f. The internal voltage of the VSC is indicated as e and the grid voltage as v. The filter current is denoted as i. A constant voltage source V_{dc} is assumed at the converter DC bus.

A circuit breaker is connected between the VSC terminals and the grid, and its state determines the operation mode of the VSC (on: grid connected, off: islanded). At VSC terminals a local load is also connected. As it will be shown later, the virtual-flux control allows the VSC to be controlled in a robust way regardless of the output filter. Obviously, the type of filter has some effect on dynamics and power quality of the converter, but unlike other GFM controls which use internal current loops, the use of capacitors is not mandatory.

GFM control block shown in Fig. 1 uses the three-phase voltages measured at the VSC terminals (v_a, v_b, v_c), the output currents in each phase (i_a, i_b, i_c), as well as the DC voltage V_{dc} to generate the switching pattern $S_{1...6}$ that determines the on and off states of the six switches of a two-level VSC. The VSC can be controlled as a PQ node, setting the active P^* and reactive Q^* power setpoints at the converter output, or as a PV node. In this case, the reactive power reference is replaced by a voltage setpoint v^*.

A. DYNAMIC EQUATIONS

The electrical equations corresponding to each of the three phases of the output filter of the VSC are as follows

$$e_k = R_f i_k + L_f \frac{di_k}{dt} + v_k \tag{1}$$

where the index k corresponds to the phases a, b, c.

The voltages v_k can be defined as the derivative of a virtual flux ψ_k at the VSC terminals as

$$v_k = \frac{d\psi_k}{dt} \tag{2}$$

Substituting (2) in (1), grouping the derivative terms and considering L_f as constant, (1) is equal to

$$e_k = R_f i_k + \frac{d}{dt}(L_f i_k + \psi_k) \tag{3}$$

where the derivative term is defined as the converter virtual-flux in each phase ψ_{kv}

$$\psi_{kv} = L_f i_k + \psi_k \tag{4}$$

which is expressed as a function of the output current and the terminal voltage v_k as

$$\psi_{kv} = L_f i_k + \int v_k dt \tag{5}$$

that is, in each phase the converter virtual-flux, ψ_{kv}, is obtained as the sum of the instantaneous current, i_k, multiplied by L_f and the integral of the voltage, v_k, measured at the output terminals of the VSC. The direct measurement of the voltage and current, indicated in Fig. 1, allows the virtual-flux ψ_{kv} to be calculated directly according to (5). The precision in the measurement of ψ_{kv} is not significantly affected by the variation of parameters, since the filter inductance L_f is a very stable magnitude.

Calculating in (4) the current as a function of the fluxes, it is obtained that

$$i_k = \frac{1}{L_f}(\psi_{kv} - \psi_k) \tag{6}$$

By substituting (6) in (3) and taking (2) into account, the system of differential equations that define the dynamics of the VSC in Fig. 1 is obtained as follows

$$\begin{aligned} \frac{d\psi_{kv}}{dt} &= e_k - \frac{1}{T_f}\left(\psi_{kv} - \psi_k\right) \\ \frac{d\psi_k}{dt} &= v_k \end{aligned} \tag{7}$$

where T_f is the filter time constant defined as L_f/R_f. As shown in (7), the state-variables are the virtual-fluxes, ψ_{kv} and ψ_k, being e_k and v_k the control variables and the input variables, respectively.

Equation (7) can be also expressed in vector form by transforming the three-phase variables, indicated with subscript k, into space vectors referred to a rotating dq-axes. These axes rotate at ω rad/s, being θ the d-axis angular position respect to a stationary reference frame. A generic spatial vector $\vec{x}$, in this rotating reference frame, is obtained from the instantaneous three-phase components x_a, x_b, x_c using the well-known expression

$$\vec{x} = x_d + jx_q = \frac{2}{3}\left(x_a + \underline{a}x_b + \underline{a}^2 x_c\right) e^{-j\theta} \tag{8}$$

where $\underline{a} = e^{\frac{j2\pi}{3}}$ and $\underline{a}^2 = e^{-\frac{j2\pi}{3}}$.

By applying the space-vector definition of (8) in (7), the following VSC dynamics equations are obtained

$$\begin{aligned} \frac{d\vec{\psi}_v}{dt} + j\omega\vec{\psi}_v &= \vec{e} - \frac{1}{T_f}\left(\vec{\psi}_v - \vec{\psi}\right) \\ \frac{d\vec{\psi}}{dt} + j\omega\vec{\psi} &= \vec{v} \end{aligned} \tag{9}$$

Note that in (9) there are two terms proportional to the angular velocity ω, as a result of the dq-axes rotation. Separating into real and imaginary components the first equation of (9) can be expressed as

$$\begin{aligned} \frac{d\psi_{dv}}{dt} + \frac{\psi_{dv}}{T_f} &= e_d + \frac{\psi_d}{T_f} + \omega\psi_{qv} \\ \frac{d\psi_{qv}}{dt} + \frac{\psi_{qv}}{T_f} &= e_q + \frac{\psi_q}{T_f} - \omega\psi_{dv} \end{aligned} \tag{10}$$

And the second one as

$$\begin{aligned} \frac{d\psi_d}{dt} &= v_d + \omega\psi_q \\ \frac{d\psi_q}{dt} &= v_q - \omega\psi_d \end{aligned} \tag{11}$$

As shown in (10), e_d controls the virtual-flux component ψ_{dv}. The dynamic relationship between these two variables responds to a first-order function neglecting the cross-coupling term $\omega\psi_{qv}$, and the resistive term $\psi_d\left(R_f/L_f\right)$, since $1/T_f = \left(R_f/L_f\right)$. This term is usually neglected as it is much smaller than the rest of terms. A similar reasoning can be made for the dynamics of ψ_{qv} and its control variable e_q in the second equation of (10).

Fig. 2 shows the block diagram corresponding to equations (10) and (11) in the Laplace s-domain.

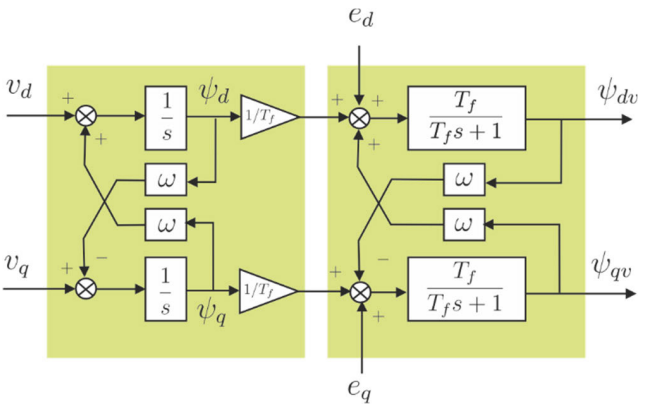

FIGURE 2. Block diagram of VSC's dynamic equations.

B. STEADY-STATE OPERATION

In this subsection, the operation of the VSC in steady state is analyzed. Considering in (9) that the derivatives are zero and the filter resistance $R_f \sim 0$ ($R_f \ll \omega L_f$) the internal voltage $\vec{e}$ can be expressed in terms of the virtual-flux as

$$\vec{e} = j\omega\vec{\psi}_v \tag{12}$$

and likewise, for the grid voltage $\vec{v}$

$$\vec{v} = j\omega\vec{\psi} \tag{13}$$

By transforming (4) into a vectorial expression using (8), and multiplying by $j\omega$ it is obtained that

$$j\omega\vec{\psi}_v = j\omega L_f\vec{i} + j\omega\vec{\psi} \tag{14}$$

Substituting (12) and (13) in (14), and given that the reactance $X_f = \omega L_f$, this equation is expressed in terms of voltages as

$$\vec{e} = jX_f\vec{i} + \vec{v} \tag{15}$$

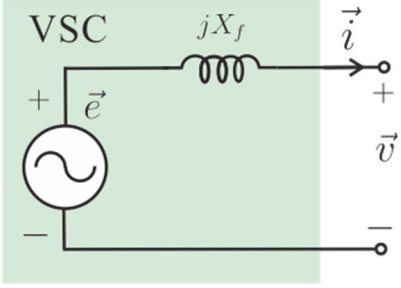

FIGURE 3. Equivalent circuit of a VSC in steady-state operation.

In other words, the VSC has an internal voltage, $\vec{e}$, equal to sum of the voltage drop in the reactance, $jX_f\vec{i}$, and the terminal voltage, $\vec{v}$. Fig. 3 shows the equivalent circuit corresponding to (15), which is analogous to the equivalent circuit of a SG represented by a voltage source behind a reactance. While the synchronous reactance of a SG is around 1 p.u, X_f in a VSC is much smaller (typically between 0.10-0.20 p.u.)

The active and reactive power injected by the VSC into the grid, can be expressed in terms of vectors $\vec{v}$ and $\vec{i}$ as follows

$$P + jQ = \frac{3}{2}\vec{v}\left(\vec{i}\right)^{\dagger} \tag{16}$$

where the operator (†) indicates complex conjugate. Calculating the current vector in (15) as a function of $\vec{v}$ and $\vec{e}$, and separating into real and imaginary part, the expression for active power, P, is obtained as

$$P = \frac{3}{2}\left(\frac{v}{X_f}\right) esin\delta \tag{17}$$

where δ is the power angle between the voltage vectors, $\vec{e}$ and $\vec{v}$. Likewise, the reactive power expression is equal to

$$Q = \frac{3}{2}\left(\frac{v}{X_f}\right)(ecos\delta - v) \tag{18}$$

Equations (17) and (18) are the classic expressions of the active and reactive power transmitted by a SG to the grid. According to (15) the internal voltage $\vec{e}$ is proportional to the virtual-flux $\vec{\psi}_v$, and therefore, its control allows to regulate the active and reactive power exchanged by the VSC.

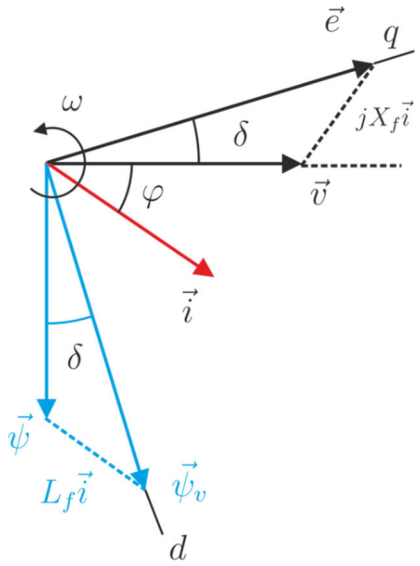

FIGURE 4. Vector diagram of the VSC in steady-state operation.

Fig. 4 shows the VSC vector diagram in steady-state operation. The voltage vector $\vec{v}$angle is taken as the angular reference. The current vector lags by an angle φ, which means that the VSC is delivering active and reactive power to the grid. The internal voltage $\vec{e}$ is calculated according to (15), its angular position corresponds to a positive power angle ($\delta > 0$) and its module, e, is higher than v, ($e > v$). A similar triangle to that representing the voltage balance in the VSC can be represented, lagging 90°, using fluxes. In this case, the virtual-flux vector is obtained as $\vec{\psi}_v = L_f\vec{i} + \vec{\psi}$, where the vector $\vec{\psi}_v$ is leading an angle δ respect to $\vec{\psi}$ and has a higher module ($\psi_v > \psi$). Both conditions, as in the triangle of voltages, determine that the VSC generates positive active and reactive power, according to (17) and (18).

In Fig. 4 it has been considered that all vectors rotate synchronously with the dq-axes at ω rad/s. The d-axis is aligned to the virtual-flux $\vec{\psi}_v$, and the q-axis to the internal voltage vector $\vec{e}$.

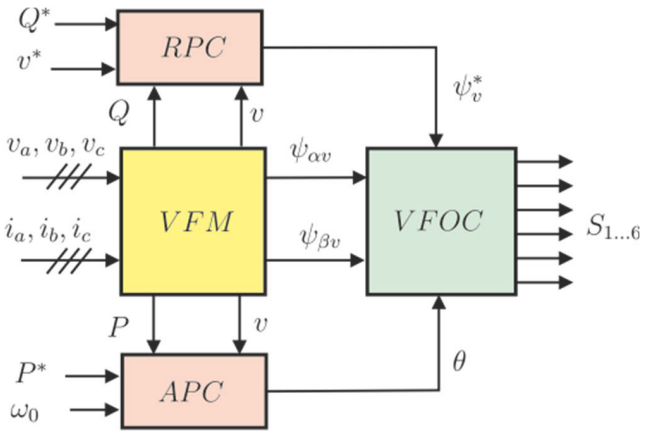

FIGURE 5. Block diagram of the virtual-flux orientation control.

III. VIRTUAL-FLUX ORIENTATION CONTROL

The VSC control scheme for the virtual-flux orientation is shown in Fig. 5. It is composed of four blocks.

In this section, the virtual-flux measurement (VFM) and its orientation control (VFOC) are presented below. The active power control block (APC) and the reactive power control block (RPC) are explained in sections IV and V, respectively.

A. VIRTUAL-FLUX MEASUREMENT

As indicated in (5) the virtual-flux in each phase, ψ_{kv}, is calculated as the product of the current i_k and the filter inductance L_f plus the integral of the voltage v_k. By applying a Clarke transformation $abc/\alpha\beta$ to these three-phase virtual-fluxes the $\alpha\beta$-components ($\psi_{\alpha v}$ and $\psi_{\beta v}$) are obtained.

$$\begin{aligned}\psi_{\alpha v} &= L_f i_\alpha + \int v_\alpha dt \\ \psi_{\beta v} &= L_f i_\beta + \int v_\beta dt\end{aligned} \tag{19}$$

where i_α, i_β and v_α, v_β are the currents and voltages $\alpha\beta$-components. To avoid using derivatives and the offset from the unknown initial conditions, the integral is approached by a first-order filter, whose cutoff frequency is close to a value of 1 Hz [73]. This gives rise to an error in the low-frequency range that is very small when the virtual flux is estimated at the fundamental frequency (50 or 60 Hz). Fig. 6 shows the Bode-plot corresponding to the response of a pure integrator $1/s$ and the first order function $1/(s+2\pi)$. As shown at 50 Hz (314.16 rad/s) the frequency response of both functions is almost the same

Fig. 7 shows the practical way to calculate the virtual-fluxes $\psi_{\alpha v}$ and $\psi_{\beta v}$. Both components are obtained by passing v_α and v_β through two filters, such as $1/(s+2\pi)$, and adding to each output the signals $L_f i_\alpha$ and $L_f i_\beta$, respectively.

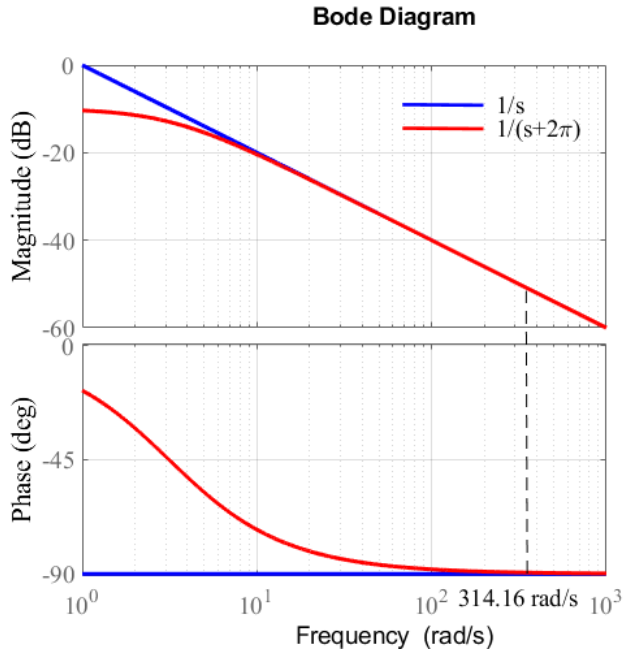

FIGURE 6. Bode-plot of the functions $1/s$, and $1/(s+2\pi)$.

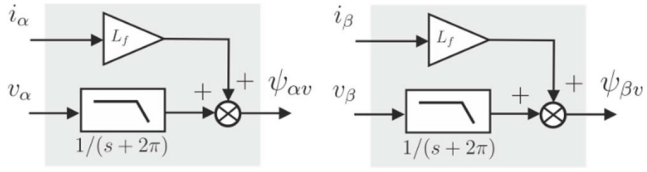

FIGURE 7. Block diagram of virtual-flux measurement.

From the $\alpha\beta$-components of voltages and currents, the active and reactive power can be calculated as

$$P = \frac{3}{2}\left(v_\alpha i_\alpha + v_\beta i_\beta\right)$$
$$Q = \frac{3}{2}\left(v_\beta i_\alpha - v_\alpha i_\beta\right) \tag{20}$$

and the voltage module as

$$v = \sqrt{v_\alpha^2 + v_\beta^2} \tag{21}$$

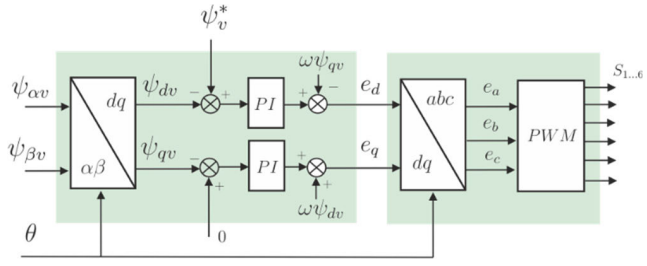

FIGURE 8. Block diagram of the virtual-flux orientation control (VFOC).

B. VIRTUAL-FLUX CONTROL

The virtual-flux orientation control scheme is shown in Fig 8. Initially, the stationary components $\psi_{\alpha v}$ and $\psi_{\beta v}$ are calculated in dq-axes by applying a $\alpha\beta/dq$ transformation, where the rotation angle, θ, is obtained from the APC block through a synchronization loop.

Once the virtual-flux components in dq-axes are obtained, a control is performed in order to keep the virtual-flux vector, $\vec{\psi}_v$, oriented to the d-axis of the rotating dq-axes. Fig. 9 shows the position of vectors $\vec{\psi}_v$ and $\vec{\psi}$, which are separated by and angle δ, and the dq-axes rotating to an angular speed ω. The angular position of the d-axis is θ respect to the α-axis.

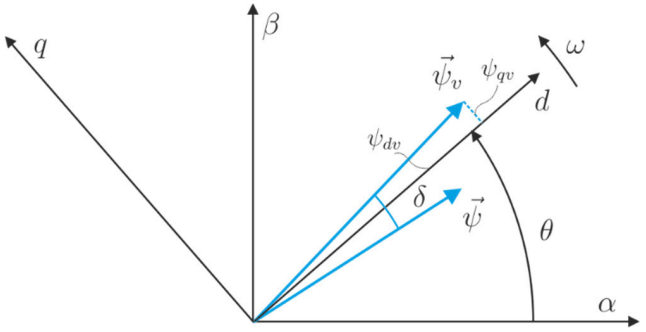

FIGURE 9. Vector diagram of the virtual-flux in $\alpha\beta$ and dq axes.

Only when the virtual-flux vector, $\vec{\psi}_v$, is aligned with the d-axis it can be said that the VSC is operating synchronously

In order to achieve this alignment, a control of the virtual-flux through the internal VSC voltage must be carried out.

As explained in section I.A (Fig. 2), the relationship between the dq-components of both magnitudes responds to a first-order function provided that the cross-coupling terms are compensated.

In Fig. 8 the control loops to regulate the virtual-flux components are shown. On the one hand, in the q-axis the reference $\psi_{qv}^* = 0$, in order to align $\vec{\psi}_v$ to the d-axis. This reference is compared to ψ_{qv} in order to obtain e_q as the output of the PI regulator and an additional feedforward signal, $\omega\psi_{dv}$, which is added to compensate the cross-coupling terms. On the other hand, e_d is obtained in a similar way by passing through a PI regulator the error between the virtual-flux module reference ψ_v^* and ψ_{dv} and compensating the cross-coupling term $-\omega\psi_{qv}$. By applying an inverse Park transformation to e_d and e_q using the angle θ, the voltage references, e_a, e_b, e_c, are obtained. From these three-phase voltages the switching pattern of the VSC, $S_{1...6}$, is calculated by using a well-known pulse with modulation (PWM) algorithm.

C. REGULATOR TUNING

The process for tuning the PI regulators is the same regardless of the axis (d or q) considered. After compensating cross-coupling terms, the transfer function $G_p(s)$ between the virtual-flux and the internal voltage in each dq components is equal to

$$G_p(s) = \frac{\psi_{dv}}{e_d} = \frac{\psi_{qv}}{e_q} = \frac{T_f}{T_f s + 1} \tag{22}$$

Fig. 10 shows the block diagram of the close-loop control system where the reference signal is any of the virtual-flux components, generically represented as ψ_{jv}^*, being the disturbance signal, as indicated in (10), ψ_j^*/L_f, where $j = d, q$.

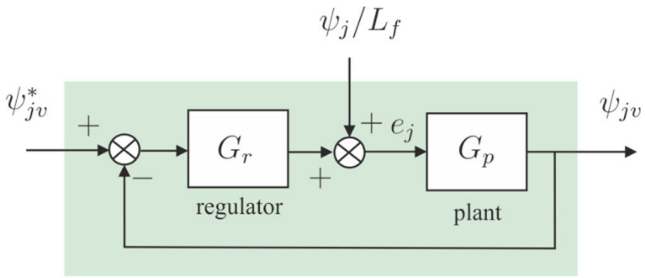

FIGURE 10. Close-loop control system.

The transfer function corresponding to the PI regulator is expressed as follows

$$G_r(s) = k_p\left(\frac{T_c s + 1}{T_c s}\right) \tag{23}$$

where k_p is the PI-gain and T_c its time constant. The open-loop transfer function is represented by the product of $G_p(s)$ and $G_r(s)$ so that

$$G(s) = G_r(s)\,G_p(s) = k_p\left(\frac{T_c s + 1}{T_c s}\right)\left(\frac{T_f}{T_f s + 1}\right) \tag{24}$$

If the time constant of the regulator is chosen equal to the time constant of the filter $T_c = T_f$, the open-loop transfer function of (24) becomes in an integral function

$$G(s) = \frac{k_p}{s} \tag{25}$$

being then, the close-loop transfer function $G'(s)$

$$G'(s) = \frac{G(s)}{1 + G(s)} = \frac{k_p}{s + k_p} = \frac{1}{\tau_i s + 1} \tag{26}$$

So that, the PI-gain is $k_p = 1/\tau_i$, being τ_i the system bandwidth. k_p is expressed in unit of s^{-1}, and in p.u. as

$$k_p\,[p.u.] = \frac{k_p\,[s^{-1}]}{\omega_0} \tag{27}$$

When $T_c = T_f$ a $k_p = 1$ p.u. means a regulator bandwidth of ω_0, that for a 50 Hz is equal to 314.16 rad/s.

D. SMALL-SIGNAL STABILITY

In (10) and (11) the dynamic equations of the VSC were presented, using as state-variables the dq-components of vectors $\vec{\psi}_v$ and $\vec{\psi}$. When these four equations are expressed in a matrix form, its state-matrix presents 2 complex-conjugated eigenvalues as shown in Fig. 11 where $\omega_0 = 314.16$ rad/s and the filter time constant, according to the parameters indicated in Appendix A, is $T_f = 159.2$ ms. As shown in Fig. 11, there are two eigenvalues over the imaginary axis corresponding to state-variables ψ_d and ψ_q whose natural frequency ω_n is

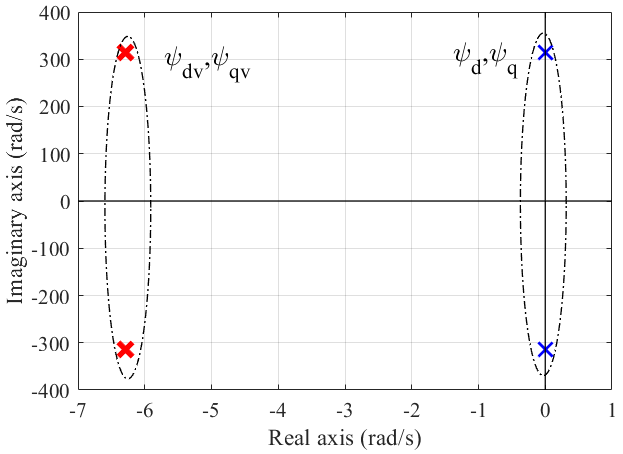

FIGURE 11. Eigenvalues corresponding to dq-components of $\vec{\psi}_v$ and $\vec{\psi}$.

equal to $\omega_0 = 314.16$ rad/s. Likewise, there are two other eigenvalues corresponding to ψ_{dv} and ψ_{qv} with a negative real part equal to 6.28 rad/s, which is the inverse value of T_f, and an imaginary value equal to $\pm\omega_0$. These eigenvalues present a small damping factor $\xi = 2\%$. As will be seen below, the virtual-flux regulator will allow increasing the damping factor of these eigenvalues.

When the virtual-flux control is implemented, the VSC output voltage vector $\vec{e}$ is calculated as a function of the virtual-flux $\vec{\psi}_v$, and its reference $\vec{\psi}_v^*$, according to the following expression

$$\vec{e} = k_p\left(\vec{\psi}_v^* - \vec{\psi}_v\right) + k_i\int\left(\vec{\psi}_v^* - \vec{\psi}_v\right)dt \tag{28}$$

where k_p is the PI-gain and k_i its integral constant that can be expressed in term of T_c as $k_i = \frac{k_p}{T_c}$. Separating (28) into real and imaginary parts, e_d and e_q are obtained as follows

$$\begin{aligned} e_d &= k_p\left(\psi_v^* - \psi_{dv}\right) + k_i\int\left(\psi_v^* - \psi_{dv}\right)dt \\ e_q &= -k_p\psi_{qv} - k_i\int\psi_{qv}dt \end{aligned} \tag{29}$$

Note that in (29) the d-component of the virtual-flux reference is equal to the reference flux module $\psi_{dv}^* = \psi_v^*$ and the q-component $\psi_{qv}^* = 0$. In order to prevent the use of integrals in the VSC dynamic equations two additional state-variables x_d, x_q are defined

$$\begin{aligned} \frac{dx_d}{dt} &= k_i\left(\psi_v^* - \psi_{dv}\right) \\ \frac{dx_q}{dt} &= -k_i\psi_{qv} \end{aligned} \tag{30}$$

So that (29) is expressed in terms of x_d, x_q as

$$\begin{aligned} e_d &= k_p\left(\psi_v^* - \psi_{dv}\right) + x_d \\ e_q &= -k_p\psi_{qv} + x_q \end{aligned} \tag{31}$$

By substituting (31) in (10) the equations corresponding to dynamics of ψ_{dv} and ψ_{qv} are now expressed as

$$\begin{aligned}\frac{d\psi_{dv}}{dt} &= -\left(\frac{1}{T_f}+k_p\right)\psi_{dv}+\omega\psi_{qv}\\ &\quad+\frac{\psi_d}{T_f}+k_p\psi_v^*+x_d\\ \frac{d\psi_{dv}}{dt} &= -\left(\frac{1}{T_f}+k_p\right)\psi_{qv}-\omega\psi_{dv}\\ &\quad+\frac{\psi_q}{T_f}+x_q\end{aligned} \tag{32}$$

In (32) the terms corresponding to ψ_{dv} in the first equation and ψ_{qv} in the second one, depend on k_p affecting directly to the system damping, as will be indicated below.

Now the VSC dynamics is represented by six state-variables, the virtual-flux components ψ_{dv}, ψ_{qv}, the grid flux components ψ_d, ψ_q, as well as x_d and x_q. Fig. 12 shows the eigenvalues loci corresponding to the VSC dynamics applying a virtual-flux orientation control with $T_c = T_f$ and k_p varying from 0 to 2 p.u, being the parameters of the system the same than before ($\omega_0 = 314.16$ rad/s and $T_f = 159.2$ ms).

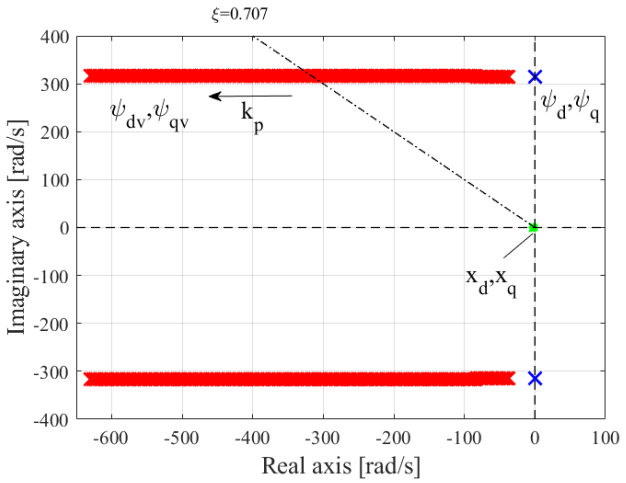

FIGURE 12. Eigenvalue loci corresponding to the virtual-flux orientation control.

The eigenvalues corresponding to ψ_d and ψ_q remain constant in the imaginary axis. However, the eigenvalues ψ_{dv}, ψ_{qv} are shifted towards the negative real axis when k_p increases. As shown in Fig. 12, the imaginary component of theses eigenvalues is constant and equal to ω_0. When $k_p = 1$ p.u. the system bandwidth matches the fundamental frequency $\omega_0 = 314.16$ rad/s and the damping factor is $\xi = 70.7\%$ (same real and imaginary components). The eigenvalues x_d and x_q remain practically constant in the negative half-plane of Fig. 12.

IV. ACTIVE POWER SYNCHRONIZATION LOOP

The active power controller (APC) is shown in Fig. 13. This controller establishes the angular position, θ, to which the virtual-flux vector $\vec{\psi}_v$ must be oriented. The inputs to APC

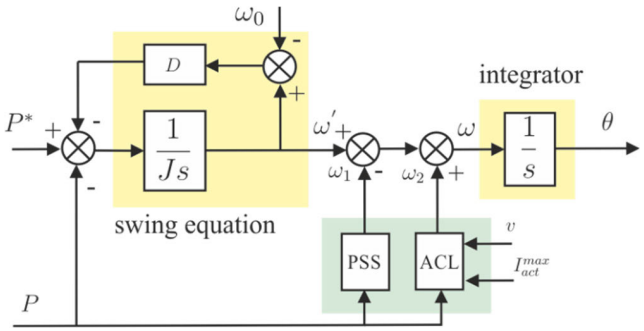

FIGURE 13. Active power controller block.

block are: the active power reference, P^*, and the frequency ω_0, as well as the active power measurement, P, and the grid voltage module, v. For the calculation of θ, the APC try to reproduce the swing equation of a SG by calculating the internal frequency ω' from the difference between the active power reference P^* and the active power P as follows

$$P^* - P = J\frac{d\omega'}{dt} + D\left(\omega' - \omega_0\right) \tag{33}$$

where J is the virtual inertia moment, that is defined as twice the inertia constant H, ($J = 2H$) when both parameters are expressed in seconds. Likewise, D is the damping factor which, in p.u., is inverse to the droop constant R ($D = \frac{1}{R}$). The rated frequency is represented by ω_0 rad/ s.

As shown in Fig. 13 the control angle θ is obtained by integration of the frequency ω, which is calculated as the internal frequency ω' minus ω_1 plus ω_2. These frequencies are the outputs of an active current limiting (ACL) block and a power system stabilizer (PSS), respectively. So that, the control angle θ is calculated as follows

$$\theta = \int \omega dt = \int \left[\omega' - \omega_1 + \omega_2\right] dt \tag{34}$$

A. ACTIVE CURRENT LIMITER

The ACL block prevents the active current I_{act} from exceeding a certain limit I_{act}^{max}. The active power is calculated according to (20), but it can also be expressed as the product of the voltage v and I_{act} as follows

$$P = \frac{3}{2} v I_{act} \tag{35}$$

I_{act} is proportional to P over v, so that the active current can be limited by limiting the active power. According to (17) the active power is proportional to $sin\delta$, being δ the power angle that is defined as

$$\delta = \theta - \omega_0 t \tag{36}$$

So, if δ is limited, P is also limited, and the way to do this is by acting on θ. Fig. 14 shows the active current limiting block. Firstly, I_{act} is obtained according to (35), as a value proportional to P divided by the module of the voltage v, whose value is previously saturated at its lower limit to a value k_+, greater than zero, in order to avoid indeterminacy when $v = 0$.

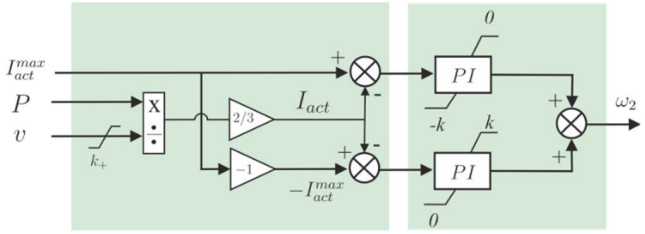

FIGURE 14. Active current limiting block.

When the active current is out of limits, e.g. $I_{act} > I_{act}^{max}$ the PI regulator generates a $\omega_2 < 0$ that is saturated to $-k$, so that the control angle θ is limited, and therefore, the active current as well. The ACL stops working when I_{act} is inside of limits. Similarly, the ACL acts generating a $\omega_2 > 0$ when I_{act} is below the lower limit $-I_{act}^{max}$.

B. APC LINEARIZED MODEL

The block diagram presented in Fig. 13 denotes the implementation of an APC, but it does not explain the synchronization process principle. For such purposes, the system is linearized around an equilibrium point. In this case equation (33) can be expressed in the s-domain as

$$\Delta\overline{P}^* - \Delta\overline{P} = (Js + D)\,\Delta\overline{\omega}' \tag{37}$$

where overlined magnitudes denote that they are expressed in p.u. Likewise, the angular increment $\Delta\delta$ can be calculated as a function of $\Delta\overline{\omega}'$ and $\Delta\overline{\omega}_g$ as follows

$$\frac{1}{\omega_0}\frac{d\Delta\delta}{dt} = \Delta\bar{\omega}' - \Delta\bar{\omega}_g \tag{38}$$

where $\Delta\bar{\omega}'$ and $\Delta\bar{\omega}_g$ are the increment of the internal frequency and the grid frequency, respectively, both expressed in p.u, and ω_0 the rated frequency in rad/s.

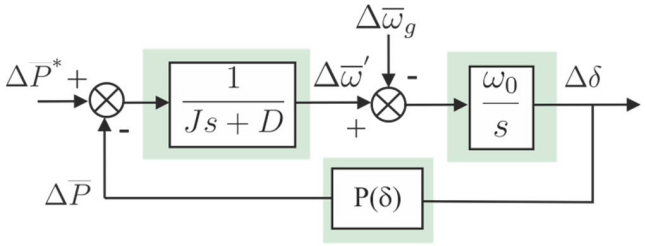

FIGURE 15. Linearized active power controller block.

The dynamic equations (37) and (38) are represented in Fig. 15 as a block diagram, where it has been considered that the active power increment ΔP is function of $\Delta\delta$.

Equation (17) denotes a non-linear relationship between the active power P and the angleδ. Considering increments in this equation, the following linear relationship for the active power and angle is obtained

$$\Delta\overline{P} = K_s\Delta\delta \tag{39}$$

where K_s is the synchronization constant whose value is calculated by applying the partial derivative of P with respect to δ (15) at the point of equilibrium ("0")

$$K_s = \left(\frac{\partial\overline{P}}{\partial\delta}\right)_0 = \left(\frac{v_0 e_0}{X_f}\right) cos\delta_0 \tag{40}$$

The (3/2) constant does not appear in this equation, since the active power $\overline{P}$ is expressed in p.u. Considering the VSC parameters in Appendix A ($X_f = 0.15$ p.u.) and assuming that, at the point of equilibrium, the internal voltage e and the grid voltage v are close to 1, ($e_0 = v_0 = 1$ p.u.) and the angle δ_0 is small ($cos\delta_0 \sim 1$), the synchronization constant is equal to K_s= 6.67 p.u. This value is significantly higher than the value for conventional SGs, which is close to 1 [74]. This causes that the power transmission is produced at lower active power angles.

When observing the block diagram of Fig. 15 and considering the synchronization constant K_s, the transfer function between $\Delta\delta$ and the reference torque $\Delta\overline{P}$, if $\Delta\bar{\omega}_g = 0$, is

$$\frac{\Delta\delta}{\Delta\bar{P}^*} = \frac{\omega_0}{Js^2 + Ds + K_s\omega_0} \tag{41}$$

which is equivalent to the oscillation equation of a SG. Reordering (41) yields

$$\frac{J}{\omega_0}s^2(\Delta\delta) + \frac{D}{\omega_0}s(\Delta\delta) + K_s(\Delta\delta) = \Delta\overline{P}^* \tag{42}$$

When equating the terms of (42) with regards to the normalized expression of a second-order function $s^2 + 2\xi\omega_n s + \omega_n^2$, it is obtained that

$$\begin{aligned}\omega_n &= \sqrt{\frac{\omega_o K_s}{J}} \\ \xi &= \frac{D}{2\sqrt{J\omega_o K_s}}\end{aligned} \tag{43}$$

where ω_n is the undamped natural frequency and ξ is the damping coefficient.

In Fig. 15, the dynamics of the VSC depend on the changes in the active power reference, $\Delta\overline{P}^*$, and the grid frequency, $\Delta\bar{\omega}_g$. The choice of the parameters D and J is not free. The damping constant D indicates the active power variation that the VSC has to produce to maintain the system synchronized when the frequency changes. For a common value of R= 0.05 p.u., the damping constant is D= 20 p.u., which denotes that, if there is a frequency variation of 0.05 p.u. (2.5 Hz in a 50 Hz grid), the VSC would increase its active power by 1 p.u. If, in (42), D is considered constant and J= 0, the response of $\Delta\overline{P}$ under changes of $\Delta\overline{P}^*$, corresponds to a first-order function with a negative pole located on the real axis

$$\sigma = -\frac{K_s\omega_0}{D} \tag{44}$$

The smaller D is, the further the pole will be from the origin and the higher the natural frequency ω_n will be. Therefore, the system's response will be faster and also more sensitive to frequency changes. Since $K_s\omega_0$ is a constant, the coefficient D is the first choice when determining the dynamics of the

active power synchronization loop. If the inertia constant J is gradually increased from 0 to greater values, the loci of the system poles is as presented in Fig. 16. Initially, the system is overdamped ($\xi > 1$), and the poles are negative and real until they meet at -2σ where $\xi = 1$. From this point, when J increases, the poles will become conjugated complexes following the path of a circumference, as shown in Fig. 16. It can be observed that this circumference has a radius of σ and the center is at $(-\sigma, 0)$. When the inertia constant increases and the value of D is held constant, the system becomes oscillatory and slows down.

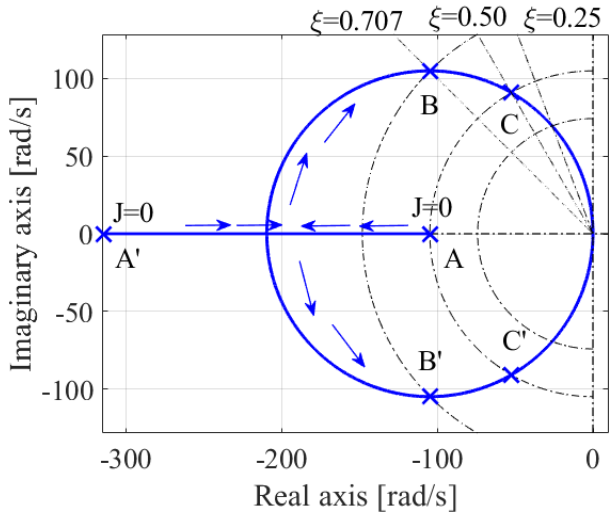

FIGURE 16. Pole loci under variation of J with D = 20 p.u.

Similarly, the transfer function between $\Delta\delta$ and $\Delta\bar{\omega}_g$ when the power reference is $\Delta\bar{P}^* = 0$ can also be achieved. In this case the power increment $\Delta\bar{P}$ is equal to

$$\Delta\overline{P} = \frac{\omega_0 K_s}{s}\left(\Delta\overline{\omega}' - \Delta\overline{\omega}_g\right) \tag{45}$$

and considering that the internal frequency increment can be expressed in term of $\Delta\overline{P}$ as

$$\Delta\overline{\omega}' = -\frac{\Delta\overline{P}}{Js + D} \tag{46}$$

Substituting (46) in (45) it is obtained that

$$\frac{\Delta\overline{P}}{\Delta\overline{\omega}_g} = -\frac{\omega_0 K_s\,(Js + D)}{s\,(Js + D) + \omega_0 K_s} \tag{47}$$

and reordering, (47) can be expressed as follows

$$\Delta\overline{P} = -\frac{\omega_0 K_s J s}{Js^2 + Ds + \omega_0 K_s}\Delta\overline{\omega}_g - \frac{\omega_0 K_s D}{Js^2 + Ds + \omega_0 K_s}\Delta\overline{\omega}_g \tag{48}$$

The first term corresponds to the inertial response where the product $s\Delta\overline{\omega}_g$ is defined as the rate of change of frequency (RoCoF), so that the power injected in steady-state ($s \to 0$) due to the inertial response is equal to

$$\Delta\overline{P}_{inertial} = -J \cdot \left(s\Delta\overline{\omega}_g\right) = -J \cdot RoCoF \tag{49}$$

Unlike this, the second term corresponds to the droop response that in steady-state is equal to

$$\Delta\overline{P}_{droop} = -D \cdot \Delta\overline{\omega}_g \tag{50}$$

In an application where the VSC presents only inertial response ($D = 0$), the second term of (48) is equal to zero and considering (39), the dynamic relationship between $\Delta\delta$ and $\Delta\overline{\omega}_g$ is expressed as follows

$$\frac{\Delta\delta}{\Delta\overline{\omega}_g} = -\frac{\omega_0 J s}{Js^2 + \omega_0 K_s} \tag{51}$$

which presents two complex-conjugated poles on the imaginary axis, being its response critically stable and oscillatory. In this case the use of a power stabilizer is required in order to avoid a poorly damped oscillatory response.

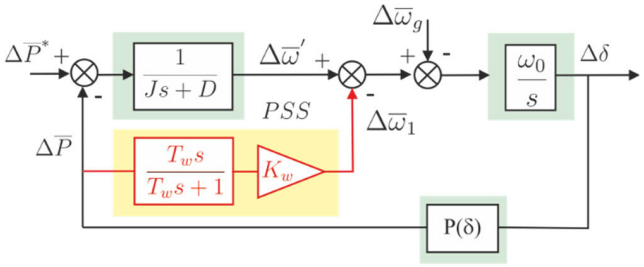

FIGURE 17. PSS block in the active power controller.

C. POWER SYSTEM STABILIZER

Fig. 17 shows the PSS block integrated on the active power controller. As explained above, a PSS is required when the swing equation of the APC is designed with a high inertia constant and a low damping gain, as when D=0. In these cases, any disturbance in the grid frequency, or any change in the active power reference, produce a poorly damped active power response that must be compensated by a PSS.

If (51) is expressed as a differential equation it is obtained that

$$J\frac{d^2(\Delta\delta)}{dt} + K_s\omega_0\Delta\delta = -\omega_0 J\frac{d\left(\Delta\overline{\omega}_g\right)}{dt} \tag{52}$$

The PSS transfer function correspond to a washout filter with gain K_w, a zero in the origin and a pole in $-1/T_w$, so that

$$\frac{\Delta\overline{\omega}_1}{\Delta\overline{P}} = -K_w\left(\frac{T_w s}{T_w s + 1}\right) \tag{53}$$

Considering the relationship between the frequency and the angle, and according to (39), equation (53) can be expressed in terms of $\Delta\delta$ as

$$T_w\frac{d^2(\Delta\delta)}{dt} = -K_w K_s T_w\omega_0\frac{d\,(\Delta\delta)}{dt} \tag{54}$$

By adding (52) and (54) the following equation is obtained

$$J'\frac{d^2\,(\Delta\delta)}{dt} + D'\frac{d(\Delta\delta)}{dt} + K_s\omega_0\Delta\delta = -\omega_0 J\frac{d\left(\Delta\overline{\omega}_g\right)}{dt} \tag{55}$$

where the new parameter J' and D' after integrating the PSS are now

$$\begin{aligned} J' &= J + T_w \\ D' &= K_w K_s (T_w \omega_o) \end{aligned} \tag{56}$$

and, (39) presents a new damping term

$$\frac{\Delta\delta}{\Delta\overline{\omega}_g} = -\frac{\omega_0 J s}{J' s^2 + D' s + \omega_0 K_s} \tag{57}$$

According to (51) J' depends on T_w, but its value is similar to J since usually J is higher than T_w. J is in the order of seconds when $T_w < 0.5$ s. So, when T_w is chosen, J' is defined and the value of D' depends directly on the PSS-gain K_w since the rests of parameters are constants. Note that when no PSS is connected ($T_w = 0$) equation (57) is the same as (51).

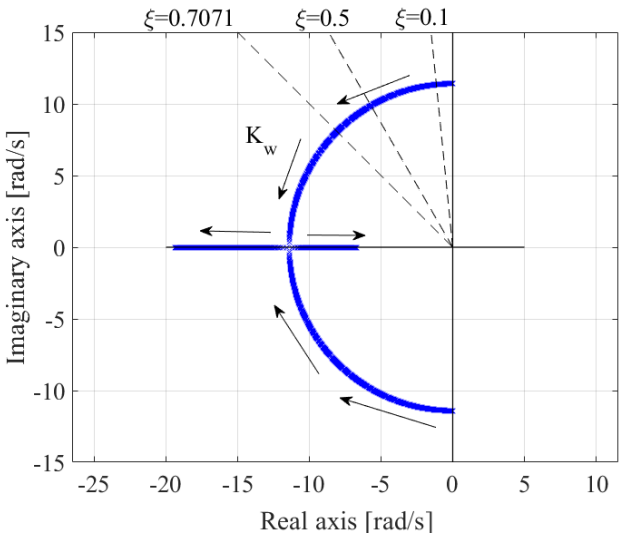

FIGURE 18. Poles loci of the transfer function $\Delta\delta/\Delta\overline{\omega}_g$ under K_w variation.

Fig. 18 shows the pole placement loci of (57) considering $J = 16$ s, $K_s = 6.67$ p.u, $T_w = 0.1s$ as a function of K_w. As shown in this figure when $K_w = 0$ two complex-conjugated poles are located on the imaginary axis and are shifted to the negative half-plane following a circumference when K_w increases up to reach a value where the poles are on the negative real axis.

As stated above, it seems essential to implement a power stabilizer to ensure an adequate response of the VSC during disturbances in the grid frequency, or when the active power reference changes. Fig. 19 shows the VSC active power response under a frequency change from 50 Hz to 47.5 Hz with a rate of change of frequency (RoCof) of 1 Hz/s. The VSC has been designed with $J = 16$ s and $D = 20$ p.u. (droop constant $R = 0.05$). As shown in that figure, for this droop value, when the frequency is reduced a 5% (2.5 Hz/50 Hz) the active power increases from 0 up to 1 p.u.

The dynamic response is very different when a PSS is used, without PSS the active power presents a high oscillatory response and exceed its rated value. On the contrary, the use

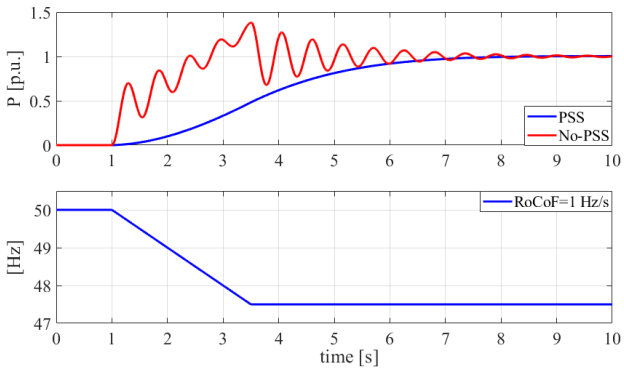

FIGURE 19. VSC active power response under a change on frequency with and without PSS. J=16 s and D=20 p.u.

of a PSS allows a smoother response of the active power but with a certain delay. The PSS has been tuning with $K_w = 1$ p.u. and $T_w = 100$ ms

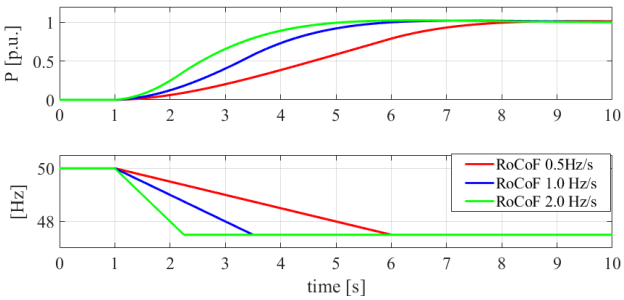

FIGURE 20. VSC active power response for different RoCoF. J=16 s, D=20 p.u and PSS.

Fig. 20 shows the VSC active power response for different RoCof when using the PSS's parameters indicated above. The lower the RoCof is, the slower the response. The active power response for a RoCof = 1 Hz/s is the same as in Fig. 19, the other two graphs correspond to the response for a higher and lower RoCof than the previous one. According to (50) a negative frequency variation of 5% and a droop D=20 p.u. gives rise to a positive power increase of 1 p.u

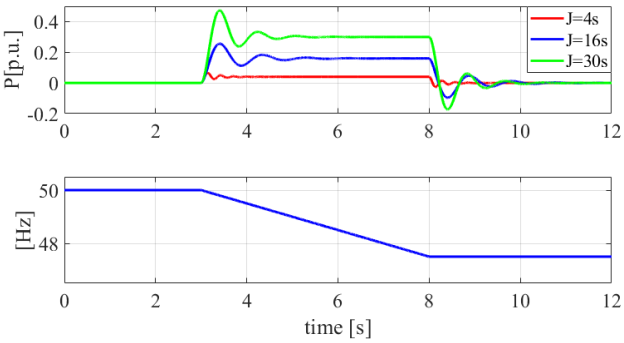

FIGURE 21. VSC inertial response (D=0 p.u). RoCof 0.5 Hz/s.

The VSC can be designed as a static synchronous compensator (SSC), so that it presents inertial response,

providing only active power during frequency variations. In this case D = 0 and according to (49) the active power increment is proportional to minus the product of J and the RoCof. Fig. 21 shows the inertial response of a VSC designed as a SSC for different J values during a frequency change with RoCof = 0.5 Hz/s. This frequency change is equivalent to a $s\Delta\overline{\omega}_g = -0.01$ p.u./s, so that according to (49) the inertial active power increment is equal to 0.3 p.u. when $J = 30$ s. As shown in Fig. 21 the VSC only exchange active power when the frequency varies, otherwise is zero. During the period of frequency variation, the active power reaches the steady state without oscillations due to the use of the PSS in the active power synchronization loop.

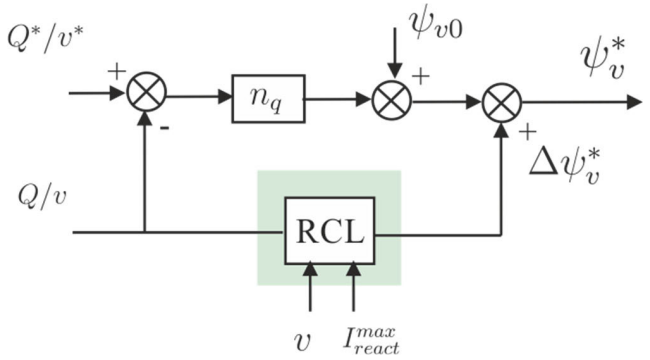

FIGURE 22. VSC reactive power controller.

V. REACTIVE POWER AND VOLTAGE CONTROLLER

Fig. 22 shows the reactive power controller that produces the virtual-flux module reference ψ_v^*. In this case, the inputs to RPC block are the reactive power reference, Q^*, or the voltage reference v^*, if the VSC is operated as a PV node. The reactive power Q or the voltage module, v, measurements are also required in order to fulfill the control. According to (18) the reactive power exchanged by the VSC mainly depends on the difference between the module of the internal voltage e and the grid voltage v. As indicated in (12) e is proportional to ψ_v^*, so the reactive power control is achieved by regulating the virtual-flux module.

Indeed, the RPC can become in a voltage controller in the case the VSC operates as a PV node. Anyway, the control principle is basically the same, it is based on the well-known droop control where the virtual-flux module reference ψ_v^* is calculated as the product of droop gain n_q and the difference between the reactive power reference, Q^*, and its actual value, Q, plus an initial virtual-flux ψ_{v0}

$$\psi_v^* = \psi_{v0} - n_q\left(Q - Q^*\right) + \Delta\psi_v^* \tag{58}$$

This equation can be interpreted as follows. When the reactive power is higher than its reference ($Q < Q^*$)ψ_v^* should be reduced in order to decrease the reactive power generated. On the contrary, ψ_v^* should be increase when ($Q > Q^*$). As shown in (58), the last term $\Delta\psi_v^*$ is a control signal that remains equal to zero when the reactive current I_{react} is inside limits. As in (35) the reactive power can be expressed as the product of v and I_{react}

$$Q = \frac{3}{2} v I_{react} \tag{59}$$

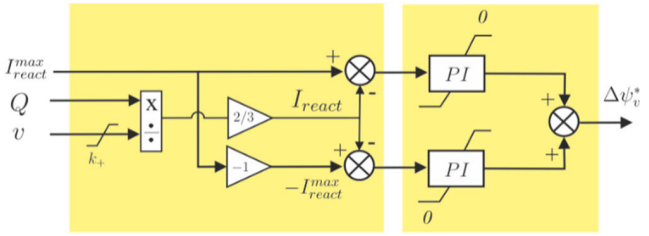

FIGURE 23. Reactive current limiting block.

The reactive current limiter (RCL) block shown in Fig. 22 calculates $\Delta\psi_v^*$ as a function of Q and v. Fig. 23 shows the logic of the RCL. Initially, I_{react} is obtained using (59), where v is previously limited to a value greater than zero in order to avoid indeterminacy when $v = 0$. Once I_{react} is calculated it is compared to I_{react}^{max}, so that when $I_{react} > I_{react}^{max}$ a PI regulator calculates a negative $\Delta\psi_v^*$ that reduce the virtual-flux module reference ψ_v^*, limiting as well I_{react}. If the reactive current is inside limits, e.g. $I_{react} < I_{react}^{max}$ the PI-regulator output is $\Delta\psi_v^* = 0$. A symmetrical regulator is used for negative values of I_{react}

VI. GRID SYNCHRONIZATION CONTROL

As in SGs, GFM-VSCs currently uses a synchronization method when connected to a grid in order to avoid overcurrent or an unstable operation in the connection instant. During synchronization the main breaker shown in Fig. 1 is open, the VSC tries to generate an instantaneous three-phase voltage system identical to the grid, so that when the breaker closes the connection current is practically zero. Fig. 24 shows the synchronization method based on the virtual-flux orientation control (VFOC).

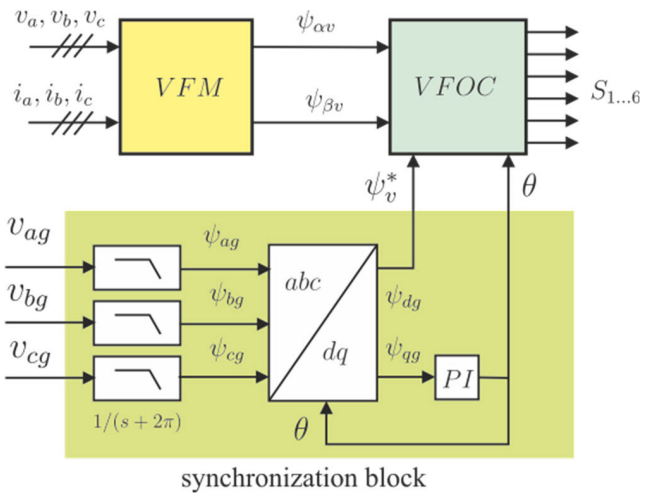

FIGURE 24. VSC synchronization block.

In this case, the synchronization is achieved when the virtual-flux vector $\vec{\psi}_v$ is oriented to the grid flux vector

$\vec{\psi}_g$ generated by the three-phase voltages v_{ag}, v_{bg}, v_{cg}, and besides the module of both vectors are the same. Firstly, the three-phase voltages of the grid are passed through a the first-order filter $1/(s + 2\pi)$ in order to obtain the grid-fluxes in each phase. From these fluxes, and applying a Park transformation, ψ_{dg} and ψ_{qg} components are obtained. Then, in order to orientate the virtual flux to the grid flux a PI regulator is used to maintain the grid flux q-component equal to zero ($\psi_{qg} = 0$). When this condition is satisfied, the control angle θ indicates the angular position of vector $\vec{\psi}_g$, being its module is equal to ψ_{dg}. On the other hand, the VFOC block shown in Fig. 24 tries to generate a virtual-flux vector whose references are: the module ψ_v^* that is equal to ψ_{dg} and the angular position θ, so that when the control objectives are achieved $\vec{\psi}_g$ and $\vec{\psi}_v$ are equal. This is the synchronization condition that ensures that the three-phase voltage systems, before and after the circuit breaker, are the same. So that, the breaker can be closed without overcurrent.

VII. CASE STUDIES AND RESULTS

This section presents the results of the study cases, which include grid synchronization, response to a grid frequency disturbance and phase jump, response to a grid fault and response to a transition from grid-tied to islanded mode. These study cases have been chosen to assess the grid-forming capabilities of the proposed control system, according to the grid code draft of National Grid ESO, ''Minimum Specification Required for Provision of GB Grid Forming Capability''. Finally, the proposed control system has been tested in a 39-node network and compared with conventional grid-forming algorithm.

FIGURE 25. Hardware in the Loop experimental set-up.

To carry out these studies, the plant illustrated in Fig. 1 has been modelled in RSCAD, for real-time simulation in the RTDS (Real Time Digital Simulator) platform, shown in Fig. 25. Tests, such as phase jumps or frequency changes, proposed by National Grid ESO, require the use of an ideal AC source in the test bench shown in Fig 1. Moreover, the control system, depicted in Fig. 1, has been implemented in a real-time dSpace platform, also shown in Fig. 25, to perform a Hardware in the Loop (HIL) real-time simulation. The parameters used in the real-time simulation of both, the plant and the control system, are given in the Table 1 and Table 2 of Appendix.

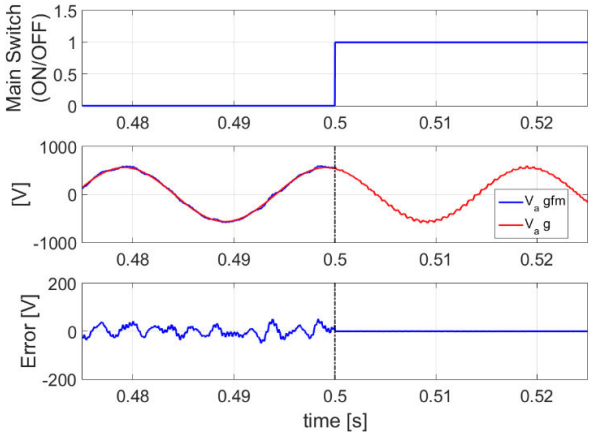

FIGURE 26. Synchronization with a LC filter.

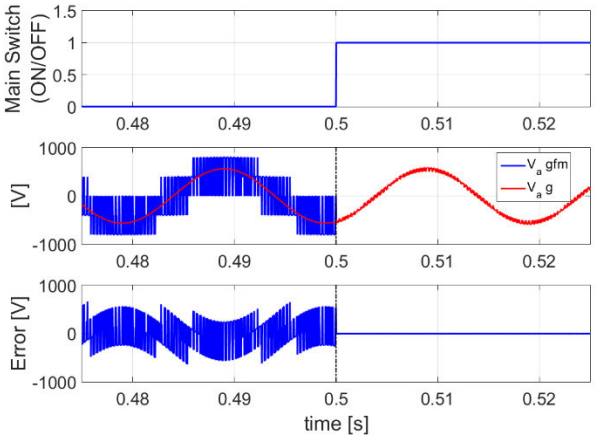

FIGURE 27. Synchronization with a L filter.

A. SYNCHRONIZATION

Before, performing any test for the assessing of the grid-forming capability, it is needed to connect the inverter to the grid. In this subsection the grid synchronization control presented above is used for such purpose. Fig 26 and 27 show the synchronization results. The difference between both figures is that in the first one the inverter uses a LC filter while in the second one, only a L filter is used. However, in both figures the state of the breaker is included. So, when the synchronization control has established a virtual flux equal to the grid flux, the breaker can be closed. Fig. 26 and 27 show the instantaneous voltages at both sides of the breaker in one phase of the system.

Also, the voltage across the breaker is shown. It is demonstrated that the virtual flux control allows the synchronization even without using a LC filter, because despite the voltage error due to the PWM, the virtual flux components are nearly constant as they are obtained by integration of such voltage.

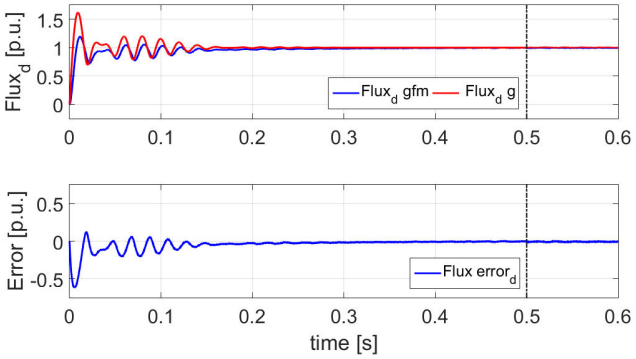

FIGURE 28. D-component of the virtual and grid fluxes during synchronization.

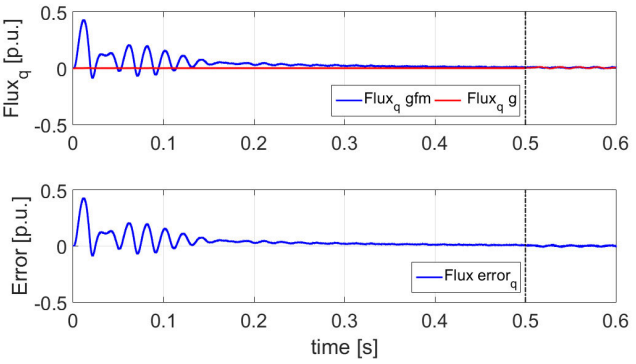

FIGURE 29. Q-component of the virtual and grid fluxes during synchronization.

This can be observed in the results presented in Fig. 28 and Fig. 29, where the direct and quadrature components of the virtual flux and the grid flux, respectively, are presented during the synchronization. Recall, that the q-components are zero, which means that both components have the same phase angle, oriented to the reference axis, while the d-components are one, which means they have the same magnitude, equal to the nominal value.

Finally, Fig. 30 shows the inverter currents during the synchronization

B. FREQUENCY AND PHASE-JUMP RESPONSE

Once the inverter is synchronized, the response to a frequency disturbance and a phase jump is obtained. The top graph of Fig. 31 shows the frequency disturbance, which consist of a frequency rise of 0.5 Hz followed by a frequency drop of 2.5 Hz, both over the nominal frequency of 50 Hz and with a ROCOF of 1 Hz/s. Fig. 31 shows the inverter response, in terms of the active and reactive power (in the middle graph) and the active and reactive current (in the bottom graph). The

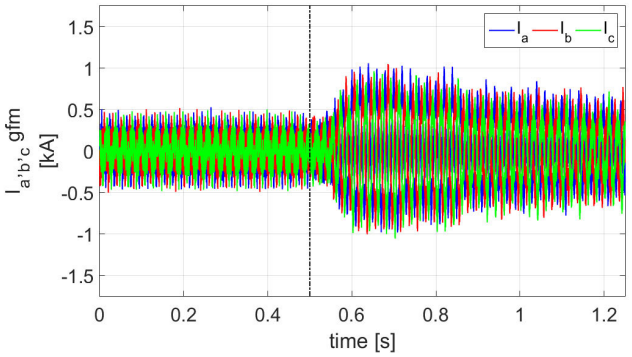

FIGURE 30. Converter currents during synchronization.

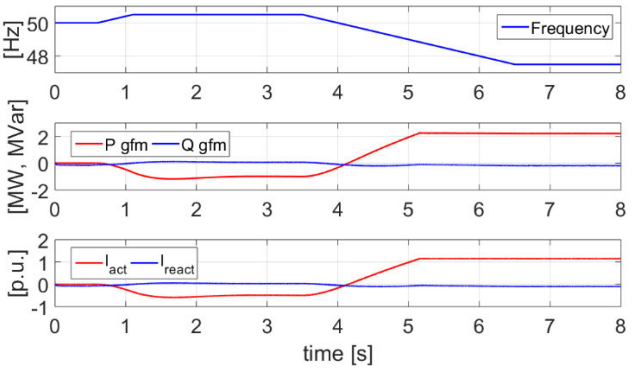

FIGURE 31. Active and reactive power and currents during a frequency disturbance.

responses show that the inverter reduces its active power and current following the frequency rise and increases its active power and current following the frequency drop. Moreover, the figure shows that the reactive power is hardly affected by the frequency disturbance, demonstrating the decoupled control of active and reactive power shown in Fig. 5. Furthermore, according to Fig. 13, the power increment following the frequency disturbance is proportional to the frequency deviation multiplied by the constant D, which was set to 50 in this test. So, the frequency rise of 1%, produces a power drop of 50%, while the frequency drop of 5% produced would produce a power increment of 250%. Nevertheless, the latter is not possible, because the inverter power (or current) cannot be increased overrated. Therefore, in order to avoid this overcurrent, the active current limiter, presented in Section IV-A has to limit current to rated. So, as shown in Fig. 31, when current reach its nominal value, it doesn't increase beyond this value, regardless frequency continues dropping.

On the other hand, Fig. 32 shows a 10° phase jump in the grid voltage. Fig. 33 shows the inverter active and reactive power and current responses to such event. This test is employed to demonstrate the inertial response capability of the proposed control system, because a phase jump means a frequency pulse. First of all, the inverter maintains the synchronism following the event, responding with a

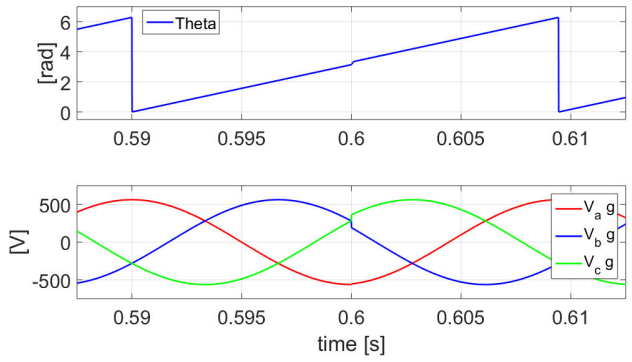

FIGURE 32. Angle and instantaneous phase voltages during a 10° phase change.

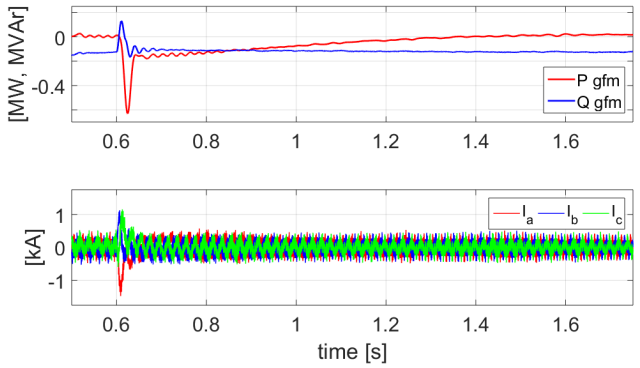

FIGURE 33. Active and reactive power and converter currents during a 10° phase change.

peak of power reduction to the phase jump. Besides, the reactive power is also affected by the event, but in a lower extend.

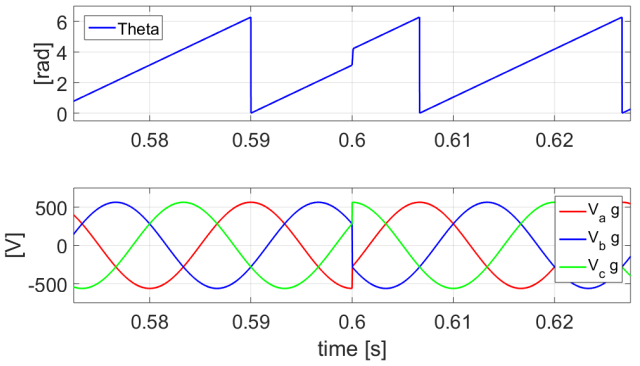

FIGURE 34. Angle and instantaneous phase voltages during a 60° phase change.

Moreover, Fig. 34 shows a 60° phase jump in the grid voltage, while Fig. 35 shows the inverter response in this case. The response is quite similar to the previous case, but in this case the active power peak is higher, as a consequence of the higher disturbance. However, both cases show the capability of the proposed grid-forming control to provide inertial response to the grid phase-jump disturbance. Fig. 34 and Fig. 35 also show the instantaneous current response.

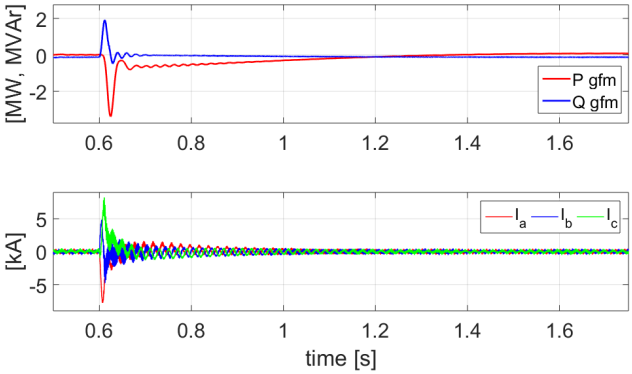

FIGURE 35. Active and reactive power and converter currents during a 60° phase change.

C. VOLTAGE RIDE-THROUGH

In this section, the response to a voltage dip is obtained, first when the voltage dip is provoked by the starting of a high-power motor and second when the voltage dip is provoked by a three-phase fault. In the first case, Fig. 36 shows the inverter terminal voltage and active and reactive current during the motor start-up at not load, followed by the loading of the motor at t = 2 s.

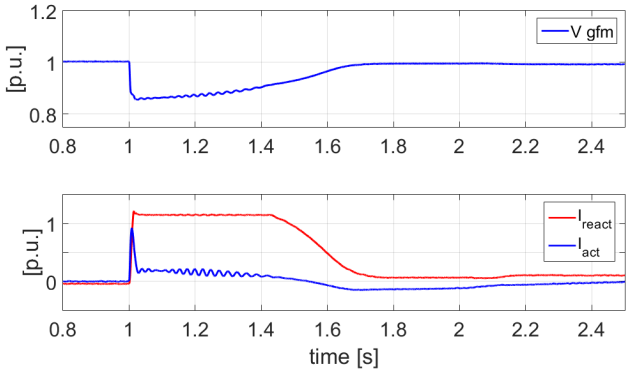

FIGURE 36. Inverter voltage and current during the motor start-up.

It can be observed that the voltage drop starts at t = 1 s and lasts about 600 ms due to the high reactive current demanded by the motor during start-up and the low grid SCR, equal to 1. However, the reactive current supplied by the inverter is limited to a maximum value of 1.15 p.u. using the reactive current limiter presented in Fig. 23.

Fig. 37 shows the instantaneous currents supplied by the inverter and grid, while Fig. 38 shows the inverter and grid active and reactive power. Finally, Fig. 39 shows the motor torque and rotational speed during the start-up and also the mechanical torque applied to the motor.

In the second case, a 20% voltage dip produced by a three-phase fault is applied to the inverter. Fig. 40 shows the voltage dip and the inverter response in terms of active and reactive current and instantaneous current as well. This response demonstrates the low voltage ride through capability of the proposed grid-forming control scheme. Also, it can be

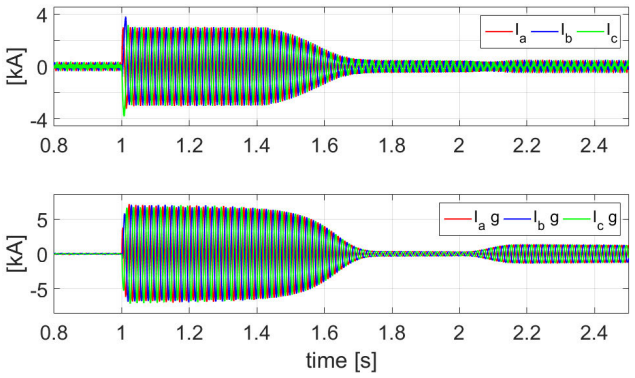

FIGURE 37. Inverter and grid instantaneous currents during the motor start-up.

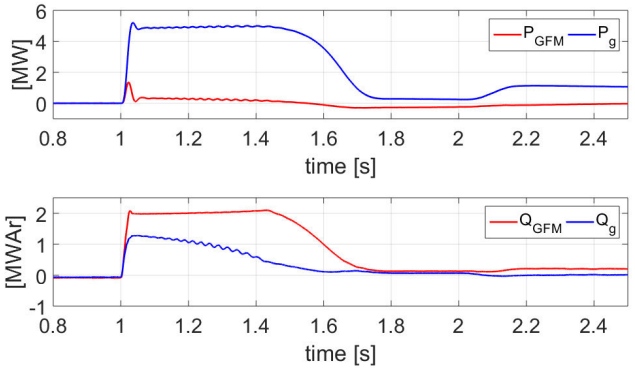

FIGURE 38. Inverter and grid active and reactive power during the motor start-up.

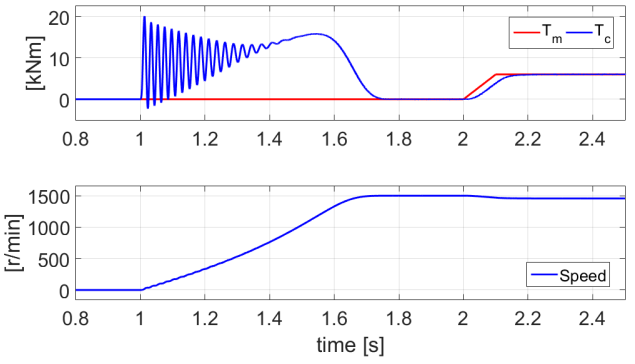

FIGURE 39. Motor torque and speed during start-up.

observed that reactive current is limited to the maximum set value during the fault, as in the previous case. It has to be noted that if the limiter was not implemented, an overcurrent would have been obtained due to the grid-forming capability of the inverter. However, this overcurrent is not allowed in the inverter and the overcurrent protection would have disconnected the inverter, preventing its LVRT capability.

D. HOT SWAP FROM GRID-CONNECTED TO ISLANDED

The transition from grid-tied to islanded mode is performed in this test. The system is first supplying a dynamic load

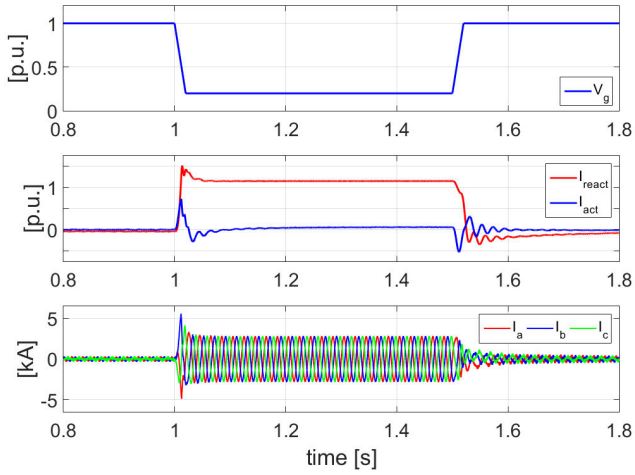

FIGURE 40. Converter currents during a three-phase voltage dip.

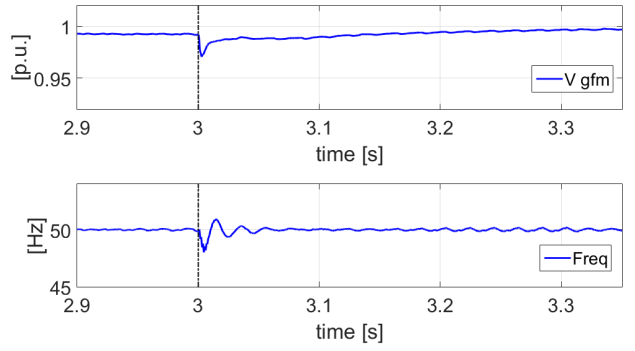

FIGURE 41. Voltage and frequency during the transition to islanded mode.

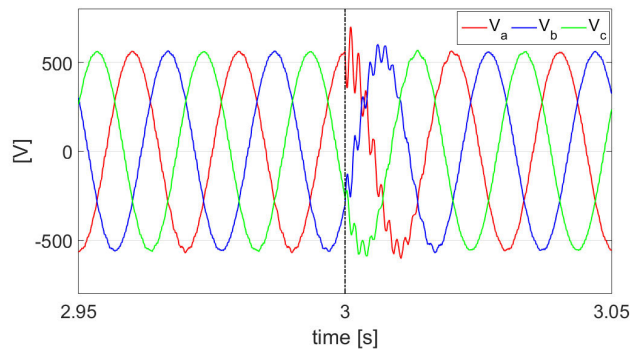

FIGURE 42. Instantaneous phase voltages during the transition to islanded mode.

demanding 1 MW and 300 kVAr. At t = 3 s, the breaker of Fig. 1 is open, separating the inverter and the load from the grid. Fig. 41 shows the inverter voltage and frequency during the transition. A disturbance can be observed in both magnitudes, but nominal voltage and frequency is recovered after a short time. Fig. 42 shows the inverter instantaneous voltages. Moreover, Fig. 43 shows the inverter and grid active and reactive power response. When the inverter is in islanded mode, it supplies the active and reactive power demanded by the load. Therefore, its active and reactive power increases

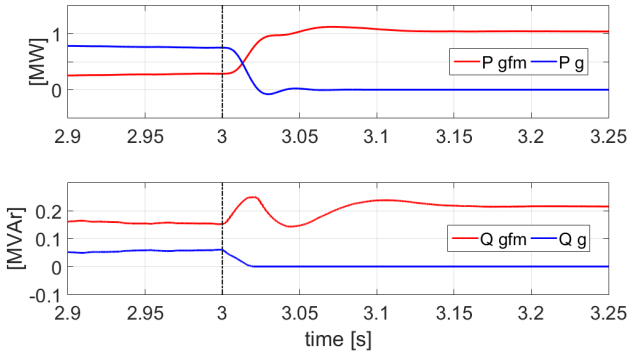

FIGURE 43. Active and reactive powers during the transition to islanded mode.

until the load demand is met. Finally, Fig. 44 shows the inverter and grid instantaneous currents, while Fig. 45 shows the motor electromagnetic torque presents a disturbance due to the voltage disturbance during the transition.

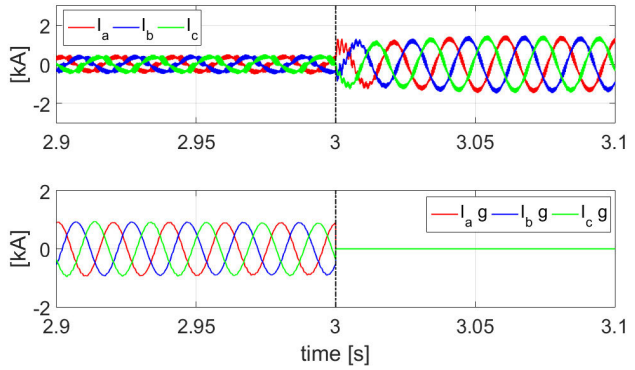

FIGURE 44. Instantaneous 3-phase currents during the transition to islanded mode.

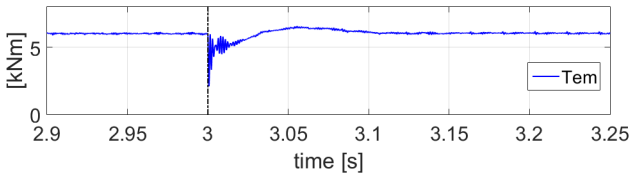

FIGURE 45. Electromechanical motor torque during the transition to islanded mode.

E. FREQUENCY AND FAULT RESPONSES IN THE IEEE 39-NODE SYSTEM

The performance of the proposed control system has been tested in the IEEE 39-node network as shown in Fig. 46, composed by 9 SGs and one GFC connected in bus 31. In order to check the frequency response of the GFC, a 140 MW load increase has been applied to the system on bus 15. Likewise, a fault on bus 12 has been applied in order to evaluate also the GFC fault response. The network parameters have been included in Table 3 of the Appendix.

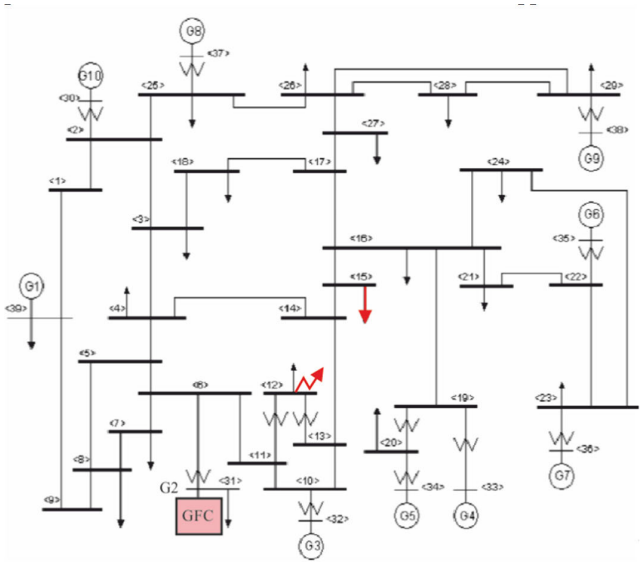

FIGURE 46. 39-node power system.

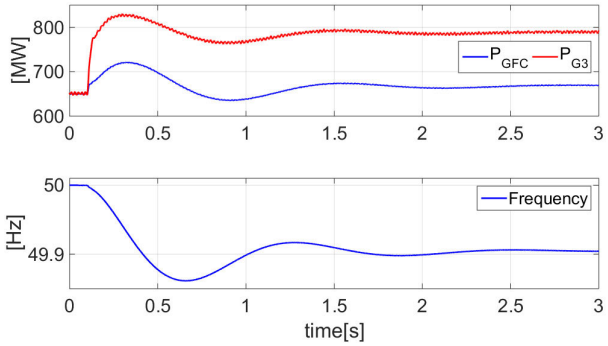

FIGURE 47. Frequency response and active power output of G3 and GFC.

Regarding the frequency response analysis all SGs have their primary regulation system disabled except G3, which will be the generator that assume the load increase. The GFC has also the primary frequency regulation disabled providing active power only during frequency variations contributing exclusively to the inertial response. Fig. 47 shows the active power response of G3 and GFC during a load step of 140 MW at t = 0.1 s. G3 has a rated power of 1000 MVA and a 2% droop constant so that increases its output from 650 MW to 790 MW with a frequency drop from 50 Hz to 49.9 Hz. During the first instants after the load change GFC increases its output power providing inertial response, supporting the system ROCOF. As G3, the initial GFC power is 650 MW and oscillates in the opposite direction to the frequency in order to reduce the ROCOF.

In order to analyze the GFC fault response during a balanced three-phase short-circuit, a 100 ms fault has been applied in bus 12. Figure 48 shows the active power exchanged by G3 and the GFC during the fault, as well as the voltage magnitude at their terminals buses 32 and 31, respectively.

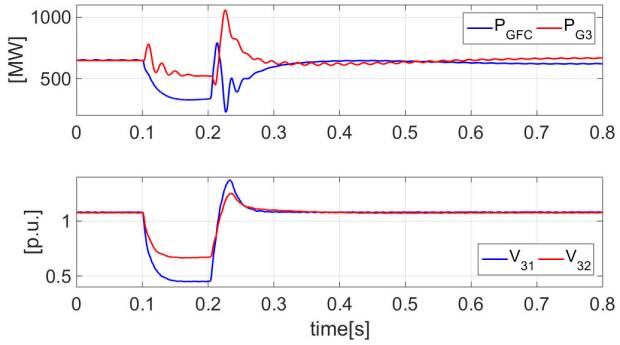

FIGURE 48. Active power output of G3 and GFC and voltages during a fault.

The fault response of the SG and the GFC differs because the during the voltage dip, the GFC current is limited to rated, in order to protect the converter. Therefore, in the GFC, active power is proportional to the voltage during the fault. After the fault is cleared, both, the SG and GFC, reach the pre-fault state in about 150 ms, proving the low voltage ride through capability of the GFC.

F. COMPARISON WITH CONVENTIONAL GRID-FORMING ALGORITHM

Finally, a comparison has been made between the performance of the proposed grid-forming control system and a conventional one using inner current loops for current limitation, as shown in Fig. 49. For comparison, the second test of section C was reproduced employing the conventional grid-forming control system, obtaining the response to a 20% voltage dip provoked by a balanced three-phase fault. In addition, the frequency disturbance shown in Fig. 31 of section B has also been reproduced for the conventional control system.

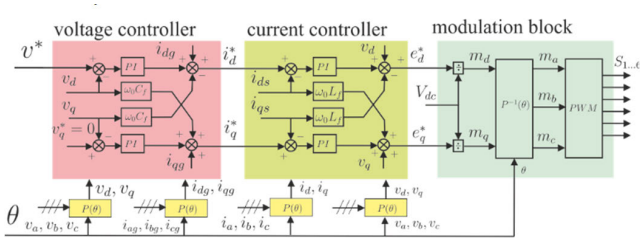

FIGURE 49. Conventional grid-forming algorithm scheme.

According to the literature, current-limited grid-forming converters can lose system stability under a voltage dip occurs. In addition, depending on the depth and the duration of the dip, the converter may not be able to re-synchronize to the grid once the fault is cleared and the voltage has been recovered. Fig. 50, shows how the same voltage dip as in section C provokes the current saturation and as result the regulator operates in open loop, losing the stability which causes that the converter is not able to re-synchronize to the grid once the fault has been cleared. This is explained by the

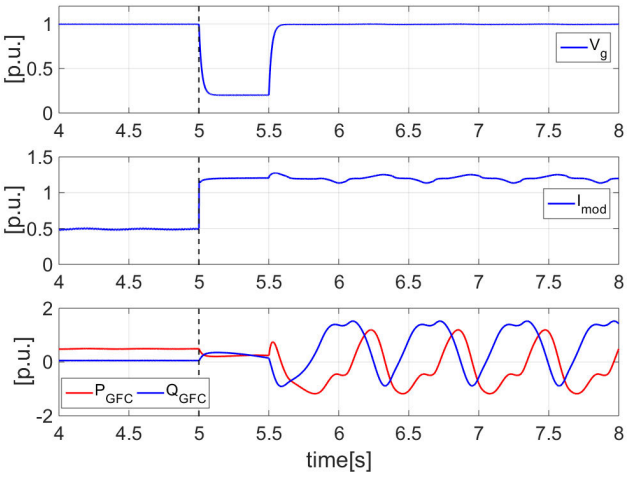

FIGURE 50. Voltage, currents and active and reactive powers of a conventional GFM converter during a dip voltage.

existence of an internal inertia in the system, which causes that the control angle obtained for regulating the active power is not related to power under current limitation. In opposition, the proposed GFC control scheme is able to re-synchronize to the grid once the fault has been cleared without losing the converter stability.

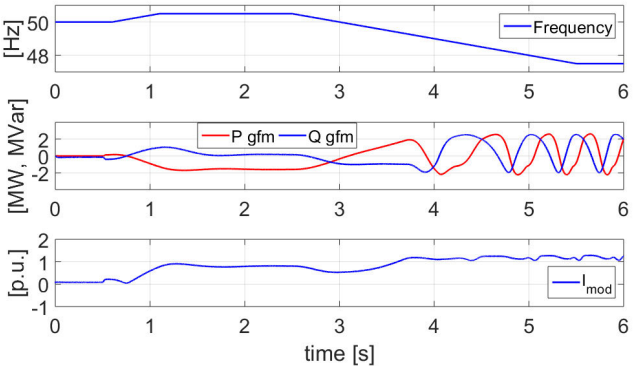

FIGURE 51. Active and reactive power and currents during a frequency disturbance.

Fig. 51 shows the response of the conventional control system to the same frequency disturbance test of Fig. 31. During the frequency rise, the system response shows that the inverter absorbs active power increasing its current without reaching the limit. However, during the frequency drop, the inverter injects active power until the current limitation is reached, which causes the regulator to operate in open loop losing again the stability.

VIII. CONCLUSION

This paper has proposed a novel grid-forming control strategy for VSCs based on the virtual flux orientation. The virtual flux is defined as the integral of the VSC internal

voltage, obtaining in this was a state variable for the VSC control. Then, the virtual flux is aligned to an axis obtained from the emulation of the synchronous generator swing equation. Through this alignment, two objectives are met, first, controlling the synchronism with the grid and, second, controlling the VSC active power. Moreover, the control of the virtual flux magnitude allows controlling the VSC reactive power.

The dynamic model of the VSC using the virtual flux was first introduced and based on this dynamic model a control scheme is derived, demonstrating its analogy to the synchronous generator. A small-signal stability analysis has also been performed to demonstrate the system stability.

The operation as a virtual synchronous machine presents two drawbacks, inherited from the SG. First, the oscillatory nature of the system with high inertia. Hence, a power system stabilizer is proposed for damping these low frequency oscillations. Second, the voltage source nature of the system leads to high short-circuit currents as a response to grid faults. Here, a current limiter is proposed as the VSC cannot withstand currents overrated.

Finally, the assessment of these capabilities has been performed using real-time hardware in the loop simulation employing comprehensive simulation models. Different tests have been performed for assessing the grid-forming capability of the proposed control scheme, including the response to frequency disturbances and voltage phase jump. Also, the low voltage ride through capability has been demonstrated, where the proposed current limiter is key. In addition, the capability to swap from grid-tied to islanded mode has also been assessed. The proposed control scheme has also been tested in a 39-node system to assess its capabilities in an electrical grid comprising SGs. Finally, a comparison has been made between the proposed control system and a traditional GFM control system.

As conclusion, the grid-forming capability of the VSC employing the proposed control scheme have been demonstrated, proving also its excellent dynamic response.

APPENDIX
RSCAD AND CONTROL SYSTEM PARAMETERS

TABLE 1. RSCAD parameters.

PARAMETERS	VALUE	UNITS
DC voltage of the VSC, V_{dc}	1200	V
Converter rated power, S_n	2	MVA
Line to line rated voltage (RMS), V_n	690	V
Filter inductance, L_f	0.113	mH
Filter resistance, R_f	0.7104	mΩ
Filter capacitance, C_f	1	mF
Nominal frequency, f_n	50	Hz
Switching frequency, f_{sw}	3	kHz
Synchronization constant, K_s	6.67	Hz/MVAr
Grid inductance, L_g	0.113	mH
Grid resistance, R_g	0.7104	mΩ
Short-circuit ratio, SCR	1	
X/R ratio	50	

TABLE 2. Control system parameters.

PARAMETERS	VALUE	UNITS
Inertia constant, H	7.5	s
Damping constant, D	50	p.u.
PSS time constant, T_w	1.2	s
PSS constant, K_w	0.01	

TABLE 3. 39-NODE system parameters.

PARAMETERS	VALUE	UNITS
Synchronous generator rated power, S_{N3}	1000	MVA
Synchronous generator rated line-line voltage, V_{N3}	16.5	kV
Frequency, f_{sg3}	50	Hz
Inertia constant, H_{sg3}	4	s
Stator leakage reactance, X_{a3}	0.14	p.u.
Unsaturated reactance, X_{d3}	1.014	p.u.
Unsaturated transient reactance, $X_{d'3}$	0.314	p.u.
Unsaturated sub-transient reactance, $X_{d''3}$	0.28	p.u.
Q-axis unsaturated reactance, X_{q3}	0.77	p.u.
Q-axis unsaturated sub-transient reactance, $X_{q''3}$	0.375	p.u.

REFERENCES

[1] *Renewable Energy Statistics*, Int. Renew. Energy Agency (IRENA), Masdar City, United Arab Emirates, 2021.
[2] J. Matevosyan, J. MacDowell, N. Miller, B. Badrzadeh, D. Ramasubramanian, A. Isaacs, R. Quint, E. Quitmann, R. Pfeiffer, H. Urdal, T. Prevost, V. Vittal, D. Woodford, S. H. Huang, and J. O'Sullivan, "A future with inverter-based resources: Finding strength from traditional weakness," *IEEE Power Energy Mag.*, vol. 19, no. 6, pp. 18–28, Nov. 2021.
[3] P. Tielens and D. V. Hertem, "The relevance of inertia in power systems," *Renew. Sustain. Energy Rev.*, vol. 55, pp. 999–1009, Mar. 2016.
[4] J. Matevosyan, B. Badrzadeh, T. Prevost, E. Quitmann, D. Ramasubramanian, H. Urdal, and R. Quint, "Grid-forming inverters: Are they the key for high renewable penetration?" *IEEE Power Energy Mag.*, vol. 17, no. 6, pp. 89–98, Nov./Dec. 2019.
[5] P. Christensen, G. K. Andersen, M. Seidel, S. Bolik, S. Engelken, T. Knueppel, and J. Fortmann, "High penetration of power electronic interfaced power sources and the potential contribution of grid forming converters," ENTSO-E, Brussels, Belgium, Tech. Rep., 2020.
[6] H. Zhang, W. Xiang, W. Lin, and J. Wen, "Grid forming converters in renewable energy sources dominated power grid: Control strategy, stability, application, and challenges," *J. Modern Power Syst. Clean Energy*, vol. 9, no. 6, pp. 1239–1256, Nov. 2021.
[7] M. C. Chandorkar, D. M. Divan, and R. Adapa, "Control of parallel connected inverters in standalone AC supply systems," *IEEE Trans. Ind. Appl.*, vol. 29, no. 1, pp. 136–143, Jan./Feb. 1993.
[8] J. M. Guerrero, L. GarciadeVicuna, J. Matas, M. Castilla, and J. Miret, "A wireless controller to enhance dynamic performance of parallel inverters in distributed generation systems," *IEEE Trans. Power Electron.*, vol. 19, no. 5, pp. 1205–1213, Sep. 2004.
[9] K. De Brabandere, B. Bolsens, J. Van den Keybus, A. Woyte, J. Driesen, and R. Belmans, "A voltage and frequency droop control method for parallel inverters," *IEEE Trans. Power Electron.*, vol. 22, no. 4, pp. 1107–1115, Jul. 2007.
[10] J. M. Guerrero, L. Garcia de Vicuna, J. Matas, M. Castilla, and J. Miret, "Output impedance design of parallel-connected UPS inverters with wireless load-sharing control," *IEEE Trans. Ind. Electron.*, vol. 52, no. 4, pp. 1126–1135, Aug. 2005.
[11] L. Huang, H. Xin, and F. Dorfler, "H ∞-control of grid-connected converters: Design, objectives and decentralized stability certificates," *IEEE Trans. Smart Grid*, vol. 11, no. 5, pp. 3805–3816, Sep. 2020.
[12] R. K. Sharma, S. Mishra, and D. Pullaguram, "A robust H∞ multivariable stabilizer design for droop based autonomous AC microgrid," *IEEE Trans. Power Syst.*, vol. 35, no. 6, pp. 4369–4382, Nov. 2020.
[13] N. Pogaku, M. Prodanovic, and T. C. Green, "Modeling, analysis and testing of autonomous operation of an inverter-based microgrid," *IEEE Trans. Power Electron.*, vol. 22, no. 2, pp. 613–625, Mar. 2007.
[14] P. Hart and B. Lesieutre, "Energy function for a grid-tied, droop-controlled inverter," in *Proc. North Amer. Power Symp. (NAPS)*, Pullman, WA, USA, Sep. 2014, pp. 1–6.
[15] S. D'Arco and J. Are Suul, "Equivalence of virtual synchronous machines and frequency-droops for converter-based MicroGrids," *IEEE Trans. Smart Grid*, vol. 5, no. 1, pp. 394–395, Jan. 2014.

[16] L. Zhang, L. Harnefors, and H. P. Nee, "Power-synchronization control of grid-connected voltage-source converters," *IEEE Trans. Power Syst.*, vol. 25, no. 2, pp. 809–820, Nov. 2010.

[17] L. Harnefors, M. Hinkkanen, U. Riaz, F. M. M. Rahman, and L. Zhang, "Robust analytic design of power-synchronization control," *IEEE Trans. Ind. Electron.*, vol. 66, no. 8, pp. 5810–5819, Aug. 2019.

[18] H.-P. Beck and R. Hesse, "Virtual synchronous machine," in *Proc. 9th Int. Conf. Electr. Power Quality Utilisation*, Oct. 2007, pp. 1–6.

[19] Y. Chen, R. Hesse, D. Turschner, and H. Beck, "Comparison of methods for implementing virtual synchronous machine on inverters," in *Proc. Int. Conf. Renew. Energies Power Quality*, 2012, pp. 1–5.

[20] J. Driesen and K. Visscher, "Virtual synchronous generators," in *Proc. IEEE Power Energy Soc. Gen. Meeting Convers. Del. Elect. Energy 21st Century*, Jul. 2008, pp. 1–3.

[21] M. Guan, W. Pan, J. Zhang, Q. Hao, J. Cheng, and X. Zheng, "Synchronous generator emulation control strategy for voltage source converter (VSC) stations," *IEEE Trans. Power Syst.*, vol. 30, no. 6, pp. 3093–3101, Nov. 2015.

[22] J. Liu, Y. Miura, and T. Ise, "Comparison of dynamic characteristics between virtual synchronous generator and droop control in inverter-based distributed generators," *IEEE Trans. Power Electron.*, vol. 31, no. 5, pp. 3600–3611, May 2016.

[23] J. Alipoor, Y. Miura, and T. Ise, "Power system stabilization using virtual synchronous generator with alternating moment of inertia," *IEEE J. Emerg. Sel. Topics Power Electron.*, vol. 3, no. 2, pp. 451–458, Jun. 2015.

[24] M. A. Torres, L. A. C. Lopes, L. A. Moran, and J. R. Espinoza, "Self-tuning virtual synchronous machine: A control strategy for energy storage systems to support dynamic frequency control," *IEEE Trans. Energy Convers.*, vol. 29, no. 4, pp. 833–840, Dec. 2014.

[25] D. Li, Q. Zhu, S. Lin, and X. Y. Bian, "A self-adaptive inertia and damping combination control of VSG to support frequency stability," *IEEE Trans. Energy Convers.*, vol. 32, no. 1, pp. 397–398, Mar. 2017.

[26] F. Wang, L. Zhang, X. Feng, and H. Guo, "An adaptive control strategy for virtual synchronous generator," *IEEE Trans. Ind. Appl.*, vol. 54, no. 5, pp. 5124–5133, Sep./Oct. 2018.

[27] M. P. N. van Wesenbeeck, S. W. H. de Haan, P. Varela, and K. Visscher, "Grid tied converter with virtual kinetic storage," in *Proc. IEEE Bucharest PowerTech*, Jun. 2009, pp. 1–7.

[28] O. Mo, S. D'Arco, and J. A. Suul, "Evaluation of virtual synchronous machines with dynamic or quasi-stationary machine models," *IEEE Trans. Ind. Electron.*, vol. 64, no. 7, pp. 5952–5962, Jul. 2017.

[29] P. Rodríguez, J. I. Candela, J. Rocabert, and R. Teodorescu, "Synchronous power controller for a generating system based on static power converters," Int. Patent WO 2012/117 131 A1, Sep. 7, 2012.

[30] S. D'Arco, J. Are Suul, and O. B. Fosso, "Control system tuning and stability analysis of virtual synchronous machines," in *Proc. IEEE Energy Convers. Congr. Exposit.*, Sep. 2013, pp. 2664–2671.

[31] J. Liu, Y. Miura, H. Bevrani, and T. Ise, "Enhanced virtual synchronous generator control for parallel inverters in microgrids," *IEEE Trans. Smart Grid*, vol. 8, no. 5, pp. 2268–2277, Sep. 2017.

[32] W. Zhang, A. M. Cantarellas, J. Rocabert, A. Luna, and P. Rodriguez, "Synchronous power controller with flexible droop characteristics for renewable power generation systems," *IEEE Trans. Sust. Energy*, vol. 7, no. 4, pp. 1572–1582, Oct. 2016.

[33] W. Zhang, A. Tarraso, J. Rocabert, A. Luna, J. Ignacio Candela, and P. Rodriguez, "Frequency support properties of the synchronous power control for grid-connected converters," *IEEE Trans. Ind. Appl.*, vol. 55, no. 5, pp. 5178–5189, Oct. 2019.

[34] X. Quan, A. Q. Huang, and H. Yu, "A novel order reduced synchronous power control for grid-forming inverters," *IEEE Trans. Ind. Electron.*, vol. 67, no. 12, pp. 10989–10995, Dec. 2020.

[35] X. Meng, J. Liu, and Z. Liu, "A generalized droop control for grid-supporting inverter based on comparison between traditional droop control and virtual synchronous generator control," *IEEE Trans. Power Electron.*, vol. 34, no. 6, pp. 5416–5438, Sep. 2019.

[36] G. N. Baltas, N. B. Lai, L. Marin, A. Tarrasó, and P. Rodríguez, "Grid-forming power converters tuned through artificial intelligence to damp subsynchronous interactions in electrical grids," *IEEE Access*, vol. 8, pp. 93369–93379, 2020.

[37] T. Qoria, E. Rokrok, A. Bruyere, B. François, and X. Guillaud, "A PLL-free grid-forming control with decoupled functionalities for high-power transmission system applications," *IEEE Access*, vol. 8, pp. 197363–197378, 2020.

[38] A. Karimi, Y. Khayat, M. Naderi, T. Dragicevic, R. Mirzaei, F. Blaabjerg, and H. Bevrani, "Inertia response improvement in AC microgrids: A fuzzy-based virtual synchronous generator control," *IEEE Trans. Power Electron.*, vol. 35, no. 4, pp. 4321–4331, Aug. 2020.

[39] Q.-C. Zhong and G. Weiss, "Synchronverters: Inverters that mimic synchronous generators," *IEEE Trans. Ind. Electron.*, vol. 58, no. 4, pp. 1259–1267, Apr. 2011.

[40] Q.-C. Zhong, P.-L. Nguyen, Z. Ma, and W. Sheng, "Self-synchronized synchronverters: Inverters without a dedicated synchronization unit," *IEEE Trans. Power Electron.*, vol. 29, no. 2, pp. 617–630, Feb. 2014.

[41] X. Wang, L. Chen, D. Sun, L. Zhang, and H. Nian, "A modified self-synchronized synchronverter in unbalanced power grids with balanced currents and restrained power ripples," *Energies*, vol. 12, no. 5, p. 923, Mar. 2019.

[42] S. Dong and Y. C. Chen, "Adjusting synchronverter dynamic response speed via damping correction loop," *IEEE Tran Energy Convers.*, vol. 32, no. 2, pp. 608–619, Jun. 2017.

[43] S. Dong and Y. Christine Chen, "A method to directly compute synchronverter parameters for desired dynamic response," *IEEE Trans. Energy Convers.*, vol. 33, no. 2, pp. 814–825, Jun. 2018.

[44] J. Roldán-Pérez, A. Rodríguez-Cabero, and M. Prodanovic, "Design and analysis of virtual synchronous machines in inductive and resistive weak grids," *IEEE Trans. Energy Convers.*, vol. 34, no. 4, pp. 1818–1828, Dec. 2019.

[45] T. Jouini, C. Arghir, and F. Dörfler, "Grid-friendly matching of synchronous machines by tapping into the DC storage," *IFAC-PapersOnLine*, vol. 49, no. 22, pp. 192–197, 2016.

[46] C. Arghir, T. Jouini, and F. Dörfler, "Grid-forming control for power converters based on matching of synchronous machines," *Automatica*, vol. 95, pp. 273–282, Sep. 2018.

[47] C. Arghir and F. Dörfler, "The electronic realization of synchronous machines: Model matching, angle tracking, and energy shaping techniques," *IEEE Trans. Power Electron.*, vol. 35, no. 4, pp. 4398–4410, Apr. 2020.

[48] B. B. Johnson, S. V. Dhople, A. O. Hamadeh, and P. T. Krein, "Synchronization of parallel single-phase inverters with virtual oscillator control," *IEEE Trans. Power Electron.*, vol. 29, no. 11, pp. 6124–6138, Nov. 2014.

[49] B. B. Johnson, S. V. Dhople, J. L. Cale, A. O. Hamadeh, and P. T. Krein, "Oscillator-based inverter control for islanded three-phase microgrids," *IEEE J. Photovolt.*, vol. 4, no. 1, pp. 387–395, Jan. 2014.

[50] B. B. Johnson, M. Sinha, N. G. Ainsworth, F. Dörfler, and S. V. Dhople, "Synthesizing virtual oscillators to control islanded inverters," *IEEE Trans. Power Electron.*, vol. 31, no. 8, pp. 6002–6015, Aug. 2016.

[51] M. Sinha, F. Dörfler, B. B. Johnson, and S. V. Dhople, "Uncovering droop control laws embedded within the nonlinear dynamics of van der pol oscillators," *IEEE Trans. Control Netw. Syst.*, vol. 4, no. 2, pp. 347–358, Jun. 2017.

[52] M. Colombino, D. Groß, and F. Dörfler, "Global phase and voltage synchronization for power inverters: A decentralized consensus-inspired approach," in *Proc. IEEE 56th Annu. Conf. Decis. Control (CDC)*, Dec. 2017, pp. 5690–5695.

[53] M. Colombino, D. Groß, J.-S. Brouillon, and F. Dörfler, "Global phase and magnitude synchronization of coupled oscillators with application to the control of grid-forming power inverters," *IEEE Trans. Autom. Control*, vol. 64, no. 11, pp. 4496–4511, Nov. 2019.

[54] D. Groÿ, M. Colombino, J. Brouillon, and F. Dörfler, "The effect of transmission-line dynamics on grid-forming dispatchable virtual oscillator control," *IEEE Trans. Control Netw. Syst.*, vol. 6, no. 3, pp. 1148–1160, Sep. 2019.

[55] M. A. Awal, H. Yu, H. Tu, S. M. Lukic, and I. Husain, "Hierarchical control for virtual oscillator based grid-connected and islanded microgrids," *IEEE Trans. Power Electron.*, vol. 35, no. 1, pp. 988–1001, Jan. 2020.

[56] M. A. Awal, H. Yu, I. Husain, W. Yu, and S. M. Lukic, "Selective harmonic current rejection for virtual oscillator controlled grid-forming voltage source converters," *IEEE Trans. Power Electron.*, vol. 35, no. 8, pp. 8805–8818, Aug. 2020.

[57] M. A. Awal and I. Husain, "Unified virtual oscillator control for grid-forming and grid-following converters," *IEEE J. Emerg. Sel. Topics Power Electron.*, vol. 9, no. 4, pp. 4573–4586, Aug. 2021.

[58] A. D. Paquette and D. M. Divan, "Virtual impedance current limiting for inverters in microgrids with synchronous generators," *IEEE Trans. Ind. Appl.*, vol. 51, no. 2, pp. 1630–1638, Mar./Apr. 2014.

[59] L. Huang, H. Xin, Z. Wang, L. Zhang, K. Wu, and J. Hu, "Transient stability analysis and control design of droop-controlled voltage source converters considering current limitation," *IEEE Trans. Smart Grid*, vol. 10, no. 1, pp. 578–591, Jan. 2017.
[60] S. Mukherjee, P. Shamsi, and M. Ferdowsi, "Improved virtual inertia based control of a grid connected voltage source converter with fault ride-through ability," in *Proc. North Amer. Power Symp. (NAPS)*, Sep. 2016, pp. 1–5.
[61] K. O. Oureilidis and C. S. Demoulias, "A fault clearing method in converter-dominated microgrids with conventional protection means," *IEEE Trans. Power Electron.*, vol. 31, no. 6, pp. 4628–4640, Jun. 2016.
[62] K. Shi, W. Song, P. Xu, Z. Fang, and Y. Ji, "Low-voltage ride-through control strategy for a virtual synchronous generator based on smooth switching," *IEEE Access*, vol. 6, pp. 2703–2711, 2017.
[63] H. Xin, L. Huang, L. Zhang, Z. Wang, and J. Hu, "Synchronous instability mechanism of P-f droop-controlled voltage source converter caused by current saturation," *IEEE Trans. Power Syst.*, vol. 31, no. 6, pp. 5206–5207, Nov. 2016.
[64] A. Tayyebi, D. Groß, A. Anta, F. Kupzog, and F. Dörfler, "Frequency stability of synchronous machines and grid-forming power converters," *IEEE J. Emerg. Sel. Topics Power Electron.*, vol. 8, no. 2, pp. 1–9, Jun. 2020.
[65] C. Glockler, D. Duckwitz, and F. Welck, "Virtual synchronous machine control with virtual resistor for enhanced short circuit capability," in *Proc. IEEE PES Innov. Smart Grid Technol. Conf. Eur. (ISGT-Europe)*, Sep. 2017, pp. 1–6.
[66] A. Gkountaras, S. Dieckerhoff, and T. Sezi, "Evaluation of current limiting methods for grid forming inverters in medium voltage microgrids," in *Proc. IEEE Energy Convers. Congr. Expo. (ECCE)*, Sep. 2015, pp. 1223–1230.
[67] F. Welck, D. Duckwitz, and C. Gloeckler, "Influence of virtual impedance on short circuit performance of virtual synchronous machines in the 9-bus system," in *Proc. Conf. Sustain. Energy Supply Energy Storage Syst. (NEIS)*, Sep. 2017, pp. 1–7.
[68] M. Zubiaga, C. Cardozo, T. Prevost, A. Sanchez-Ruiz, E. Olea, P. Izurza, S. H. Khan, and J. Arza, "Enhanced TVI for grid forming VSC under unbalanced faults," *Energies*, vol. 14, no. 19, p. 6168, Sep. 2021.
[69] T. Qoria, F. Gruson, F. Colas, X. Guillaud, M.-S. Debry, and T. Prevost, "Tuning of cascaded controllers for robust grid-forming voltage source converter," in *Proc. Power Syst. Comput. Conf. (PSCC)*, Jun. 2018, pp. 1–7.
[70] J. Hu, J. Zhu, D. G. Dorrell, and J. M. Guerrero, "Virtual flux droop method—A new control strategy of inverters in microgrids," *IEEE Trans. Power Electron.*, vol. 29, no. 9, pp. 4704–4711, Sep. 2014.
[71] M. Malinowski, M. P. Kazmierkowski, S. Hansen, F. Blaabjerg, and G. D. Marques, "Virtual-flux-based direct power control of three-phase PWM rectifiers," *IEEE Trans. Ind. Appl.*, vol. 37, no. 4, pp. 1019–1027, Jul. 2001.
[72] Y. Cho and K.-B. Lee, "Virtual-flux-based predictive direct power control of three-phase PWM rectifiers with fast dynamic response," *IEEE Trans. Power Electron.*, vol. 31, no. 4, pp. 3348–3359, Apr. 2016.
[73] M. Silva, C. Silva, and S. Diaz, "Rotor flux vector control of DFIG without currents rotor sensor," in *Proc. IEEE Int. Electric Mach. Drives Conf.*, May 2009, pp. 881–887.
[74] P. Kundur, *Power System Stability and Control*. Palo Alto, CA, USA: Electric Power Research Institute, 2007.

JOSÉ LUIS RODRÍGUEZ-AMENEDO (Senior Member, IEEE) received the M.S. degree in industrial engineering from the University Polytechnic of Madrid, in 1994, and the Dr-Ing. (Ph.D.) degree in industrial engineering from the University Carlos III of Madrid, in 2000. From 1999 to 2000, he was a Technology Wind Turbine Manager at Iberdrola Engineering, and a Wind Energy Manager at Iberdrola Renewables, from 2001 to 2003. In 2003, he joined as an Associate Professor with the Electrical Department, University Carlos III of Madrid. From 2008 to 2011, he requested an academic leave of absence for founding the technological companies Energy to Quality (E2Q) and Wind to Power Systems (W2PS). His research interests include renewable energy integration into the grid, power electronic converter control, HVDC transmission systems, and energy storage solutions.

SANTIAGO ARNALTES GÓMEZ received the Ph.D. degree in industrial engineering from the Polytechnical University of Madrid, in 1993. He is currently a Full Professor of electrical engineering with the Carlos III University of Madrid. His research interests include modeling, simulation, and control of renewable energy systems and energy storage systems.

MARKEL ZUBIAGA was born in 1983. He received the B.Sc. and M.Sc. degrees in electrical engineering and the Ph.D. degree from the University of Mondragon, Mondragon, Spain, in 2005, 2007, and 2011, respectively. Since 2011, he has been working as a Research and Development Engineer with the Renewable Energy Systems Department, Ingeteam. His research interests include power electronics, renewable energy systems, energy transmission systems, power systems with high penetration of power converters, and grid forming control.

PEDRO IZURZA-MORENO was born in Bilbao, Spain, in 1982. He received the M.Sc. degree in automation and industrial electronics from Mondragon University, Mondragon, Spain, in 2007. In 2007, he joined the Industrial and Marine Drives Department, Ingeteam Technology, S.A., Zamudio, Spain, where he was involved in research on high-power inverters, especially on vector control, firmware design and programming, pulse width modulation (PWM), space-vector PWM, selective harmonic elimination modulation, and three-level neutral-point-clamped inverters.

JOSEBA ARZA received the B.Sc. degree in power electronics from the University of Mondragon, Spain, in 1994, the M.Sc. degree in electric machines from École Nationale Supérieure d'Ingénieurs Électriciens de Grenoble, France, in 1996, and the Ph.D. degree in drives control and regulation from the Institut National Polytechnique de Grenoble, France, in 1999. In 1999, he joined Ingeteam as a Research and Development Engineer of control and regulation for industry, marine, traction, wind, solar, and grid applications. Since 2016, he has been the Managing Director with Ingeteam Research and Development Europe, S.L.

JUAN DOLADO FERNÁNDEZ received the B.S. degree in electronic engineering and industrial automation from the University of Alcalá, in 2018, and the M.S. degree in automation and robotics from the University Polytechnic of Madrid, in 2020. He is currently pursuing the Ph.D. degree in electrical engineering with the University Carlos III of Madrid. Since 2021, he has been a Predoctoral Researcher with the Department of Electrical Engineering, University Carlos III of Madrid. His research interests include control of power electronic converters, grid-forming converters, and power system stability.